Structures in Solutions from Joint Experimental-Computational Analysis: Applications to Cyclic Molecules and Studies of Noncovalent Interactions

4 **AUTHORS**, INCLUDING:

Abil E Aliev
University College London
269 PUBLICATIONS **1,643** CITATIONS

SEE PROFILE

Frank D King
University College London
125 PUBLICATIONS **2,316** CITATIONS

SEE PROFILE

Structures in Solutions from Joint Experimental-Computational Analysis: Applications to Cyclic Molecules and Studies of Noncovalent Interactions

Abil E. Aliev,* Zakirin A. Mia, Harmeet S. Khaneja, and Frank D. King

Department of Chemistry, University College London, 20 Gordon Street, London WC1H 0AJ, United Kingdom

S *Supporting Information*

ABSTRACT: The potential of an approach combining nuclear magnetic resonance (NMR) spectroscopy, molecular dynamics (MD) simulations, and quantum mechanical (QM) calculations for full structural characterizations in solution is assessed using cyclic organic compounds, namely, benzazocinone derivatives **1**−**3** with fused five- and eight-membered aliphatic rings, camphoric anhydride **4**, and bullvalene **5**. Various MD simulations were considered, using force field and semiempirical QM treatments, implicit and explicit solvation, and high-temperature MD calculations for selecting plausible molecular geometries for subsequent QM geometry optimizations using mainly B3LYP, M062X, and MP2 methods. The QM-predicted values of NMR parameters were compared to their experimental values for verification of the final structures derived from the MD/QM analysis. From these comparisons, initial estimates of quality thresholds (calculated as rms deviations) were 0.7−0.9 Hz for $^3J_{HH}$ couplings, 0.07−0.11 Å for interproton distances, 0.05−0.08 ppm for ^1H chemical shifts, and 1.0−2.1 ppm for ^{13}C chemical shifts. The obtained results suggest that the accuracy of the MD analysis in predicting geometries and relative conformational energies is not critical and that the final geometry refinements of the structures selected from the MD simulations using QM methods are sufficient for correcting for the expected inaccuracy of the MD analysis. A unique example of $C(sp^3)$—H···$N(sp^3)$ intramolecular noncovalent interaction is also identified using the NMR/MD/QM and the natural bond orbital analyses. As the NMR/MD/QM approach relies on the final QM geometry optimization, comparisons of geometric characteristics predicted by different QM methods and those from X-ray and neutron diffraction measurements were undertaken using rigid and flexible cyclic systems. The joint analysis shows that intermolecular noncovalent interactions present in the solid state alter molecular geometries significantly compared to the geometries of isolated molecules from QM calculations.
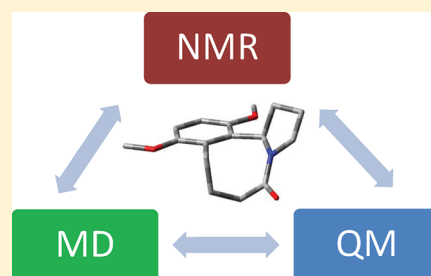
1. INTRODUCTION

While protein structure determination based on the analysis of nuclear magnetic resonance (NMR) data and computations is a well-established technique,[1] the use of NMR spectroscopy for full three-dimensional structural characterizations of small organic molecules has not been fully explored. One of the underlying reasons for slow progress in this area is that only small nuclear Overhauser effects (NOEs) are available for organic molecules with molecular weights less than ∼1000, limiting the number of available NMR constraints for structure refinements.[2] Another reason is that X-ray diffraction (XRD) has traditionally been applied for full structure characterizations of small molecules, even though it is well-recognized that the molecular structure can change on going from the solid state into solution and that not all molecules can grow into single crystals as needed for XRD. Depending on the solvent used for growing single crystals, a given molecule can also form different tautomers or conformers, which clearly restricts researchers' ability to characterize various plausible three-dimensional geometries for a given combination of atoms and their relative stability in solutions.

Clearly, structure determinations in solution are needed because the majority of synthetic routes employed in chemistry involve solution-state reactions. Similarly, understanding of the pharmacological activity of small molecules requires detailed knowledge of their structures in solution. Furthermore, when transferred from the solid state into solution, molecules obtain the freedom to sample various conformational states with different frequencies. There is, thus, a need to extend full three-dimensional structure predictions to small molecules in solution. One clear advantage compared to proteins is that small molecules are within reach of first-principles calculations, including computations of NMR parameters.[3,4]

With these considerations in mind, we recently applied a combined approach comprising NMR spectroscopy, molecular dynamics (MD) simulations, and quantum-mechanical (QM) calculations for the structure and dynamics predictions of open-chain peptides.[5] The results showed that this approach, in which each of the techniques compensates for the deficiencies of the

other two, allows substantial enhancement of the amount and quality of structural information that can be extracted from NMR spectra. In principle, the combined NMR/MD/QM method has the potential to become a universally applicable technique for full structural characterization in solution, where currently no reliable methodology is available. However, among the three techniques used, the accuracy of the MD stage of analysis is less satisfactory compared to that of either QM methods or NMR spectroscopy,[6] especially in the case of compounds for which MD force fields have not been optimized extensively.

Herein we assess the potential of the combined experimental-computational approach using cyclic organic molecules 1−5.
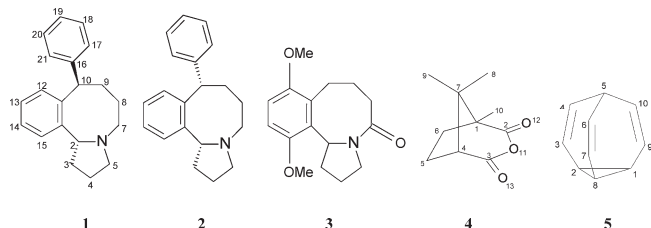
Two main objectives of this work are to assess how well the NMR/MD/QM structures agree with those from diffraction measurements in the solid state and how critical the accuracy of the MD force field is when combined with the subsequent QM analysis. Thus, cyclic systems are more suitable for the purposes of this work than open-chain molecules. Also, 1−5 represent typical examples of organic molecules for which MD force fields have not been developed as extensively as for proteins and peptides. The fact that organic species cannot be presented as sequences of a relatively small number of building units (such as proteins are formed from amino acid residues) greatly obscures optimizations of their MD force field parameters. Therefore, rather than improving MD force field parameters, we focus on the QM step of the NMR/MD/QM analysis to assess whether the final QM refinements of molecular geometries can correct for the expected inaccuracy of the MD simulations. Essentially, the objective of the MD step of the analysis is reduced to identifying possible molecular geometries. When necessary, short high-temperature MD simulations are also carried out to identify conformations with very small populations, not detected by ambient-temperature MD simulations over long time scales.

From a structural point of view, benzazocinone derivative 1 presents a unique example of C(sp^3)—H···N(sp^3) intramolecular interaction. For comparative studies, we also determined the structure and dynamics of 2, which is isomeric to 1. In addition, benzazocinone 2 is conformationally more heterogeneous than 1, allowing for an assessment of the scope and limitations of the NMR/MD/QM analysis.

For a more detailed assessment of the combined approach, we have considered amide 3, which, unlike amines 1 and 2, is a solid and has been characterized using single-crystal XRD.[7] For the same reason, we also considered camphoric anhydride 4 and bullvalene 5, for which both single-crystal X-ray and neutron diffraction structures have been reported.[8−11] Note that, unlike XRD, neutron diffraction is capable of providing accurate positions of hydrogen atoms. More importantly, 4 and 5 present examples of rigid cyclic systems. No large-amplitude conformational changes are expected in 5, whereas only methyl groups undergo reorientations in 4. The availability of the solid-state structures of 3−5 provides a reference point for comparisons, because, in principle, cyclic systems are more likely to retain their

solid-state molecular geometries in solution[12] or undergo only slight changes compared to open-chain systems. Thus, comparisons of experimental diffraction data in the solid state and QM-optimized geometries could provide insight into the reliability of geometries predicted by the NMR/MD/QM approach, as well as the significance of intermolecular interactions and crystal packing effects in altering intramolecular geometries in the solid state.

Unlike proteins and peptides, for which verifications of derived structures mainly rely on empirical schemes for calculating NMR J couplings and chemical shifts,[6,13] a wide range of first-principles computations are available in the case of small molecules, thus enabling a more rigorous validation against experimental data. Herein, we focus on three types of parameters derived from NMR measurements (NOEs, J couplings, and chemical shifts) for final verification of the predicted structures and their use for estimating relative conformational stabilities. The final verification stage can be considered as the key stage of the analysis, as it reveals the level of confidence in the structures obtained. In the absence of other means of establishing structures in solution, we consider the structure as reliable provided that all of the experimental parameters—internuclear distances, J couplings, and chemical shifts—are reproduced by QM calculations with root-mean-square (rms) deviations from experimental values not exceeding certain thresholds. Clearly, the larger the number of different experimental NMR parameters considered, the higher the confidence level in the derived structures and their conformational dynamics. The actual values of the "quality" thresholds calculated as rms deviations from experimental values are determined by the experimental errors, as well as by the accuracy of the QM protocols and a posteriori correction schemes used. We provide initial estimates of such thresholds in this work for different types of parameters derived from NMR experiments.

2. EXPERIMENTAL SECTION

2.1. NMR Measurements. Solution ^{1}H NMR spectra were recorded on Bruker AVANCE III 600 and AVANCE III 400 NMR spectrometers equipped with a Bruker 5-mm cryoprobe (600 MHz) and a room-temperature probe (400 MHz). Data acquisition and processing were performed using standard Bruker TopSpin (version 2.1) software. ^{1}H and ^{13}C chemical shifts relative to tetramethylsilane (TMS) were calibrated using the residual solvent peaks (^{1}H 7.26 ppm and ^{13}C 77.15 ppm in CDCl$_3$ and ^{1}H 5.32 ppm and ^{13}C 53.84 ppm in CD$_2$Cl$_2$).[14] Uncertainties in measured values of ^{1}H and ^{13}C chemical shifts are typically ±0.01 and ±0.05 ppm, respectively. Unless otherwise specified, spectra were recorded at 298 K. High- and low-temperature calibrations were carried out using standard samples of 80% 1,2-ethanediol in dimethyl-d_6 sulfoxide (DMSO-d_6) and 4% CH$_3$OH in CD$_3$OD, respectively.[15]

Accurate values of experimental ^{1}H−^{1}H coupling constants were determined from iterative full line shape analyses of ^{1}H NMR spectra using the gNMR program.[16] Up to 14 inequivalent spin sites were included in the full line shape analysis of ^{1}H NMR spectra. For the values of J couplings determined from the full line shape analysis of 1−3, the standard deviation is estimated to be less than 0.07 Hz.

Nonlinear least-squares fittings of the vicinal ^{3}J couplings of the five-membered pyrrolidine ring in 1−3 (see sections 3.4 and 3.5) was carried out using a Fortran program based on an approach similar to that described previously,[17] but using a

1094

dx.doi.org/10.1021/jp211083f |J. Phys. Chem. A 2012, 116, 1093−1109

simulated annealing algorithm,[18] and empirically optimized Karplus-type eqs 8C and 8D of Haasnoot et al.[19] These equations contain terms accounting for the differences in electronegativities of α- and β-substituents and, hence, are better suited for the analysis of the ^3J couplings of the pyrrolidine ring than the original Karplus equation.[20] The rms deviation, defined as $(1/N)\Sigma_{i=1}^{N}(J_{exp}^{i} - J_{calc}^{i})^2$, was used as a figure-of-merit function, where J_{exp}^{i} and J_{calc}^{i} are experimental and calculated couplings, respectively, and N is the number of different J couplings available.

Two-dimensional NOE measurements were undertaken to establish the spatial proximities of the protons.[2] Dissolved oxygen was removed from the $CDCl_3$ solutions of $\mathbf{1}-\mathbf{3}$ used in NOE measurements. Internuclear ^1H—^1H distances were determined from two-dimensional NOE spectra, using a simplified version of the growth rates method,[21] in which cross-peak intensities measured at a single mixing time (600 ms) are used. Cross-peaks showing artifacts due to the evolution of zero quantum coherence of J-coupled spins during the mixing time[2a,b] were excluded from consideration. Based on the error analysis of two-dimensional NOE spectroscopy (NOESY) measurements reported previously,[6n] the standard deviations for distance measurements are typically 10% of the corresponding mean values. The satisfactory performance of the simplified growth rates method is supported by the results obtained for the conformationally homogeneous benzazocinone $\mathbf{1}$ in this work, which shows rms deviations of 0.070−0.077 Å compared to interproton distances from three different sets of QM calculations (Table S41, Supporting Information). To verify the reliability of the results using the simplified growth rates method, the intensity ratio method was employed previously,[2c,5,6n] which relies on the ratio of cross-peak and diagonal-peak intensities. As the results from two methods were in good agreement within the experimental errors involved, we used only the growth rates method in this work.

2.2. MD Calculations. The initial geometries of $\mathbf{1}-\mathbf{3}$ were prepared using available J couplings and NOEs (as well the XRD data in the case of amide $\mathbf{3}$),[7] which were then optimized using molecular mechanics (MM) calculations[22] prior to MD simulations. Three different types of MD simulations were carried out using AMBER (version 10):[23] (i) general Amber force field (GAFF)[24] MD simulation for a single solute molecule ($\mathbf{1}$, $\mathbf{2}$, or $\mathbf{3}$) with the "standard" pairwise generalized Born solvation model for implicit solvent simulations[25] in chloroform (dielectric constant 4.7113), (ii) self-consistent charge density functional tight-binding (SCC-DFTB)[26] MD simulation for a single solute molecule ($\mathbf{1}$, $\mathbf{2}$, or $\mathbf{3}$) with the standard pairwise generalized Born solvation model for implicit solvent simulations[25] in chloroform, and (iii) GAFF MD simulation with explicit solvation of a single solute molecule ($\mathbf{1}$, $\mathbf{2}$, or $\mathbf{3}$) in chloroform (236−241 solvent molecules, box volume $\approx$ 58000 Å^3). The AM1-BCC (bond charge correction)-derived charges were used in GAFF MD calculations i and iii.[27] Simulations i and ii were of the NVT type, whereas simulations iii employed NPT calculations. The temperature was controlled to 300, 500, or 1000 K with the Langevin algorithm. In NPT calculations, the pressure at 1 bar was controlled using an isotropic position scaling with a 5-ps time constant. The nonbonded cutoff distance was set to 12.0 Å in MD simulations i and ii and to 10.0 Å in MD simulations iii. These cutoff distances are either similar to or longer than those used previously.[6i,l] After a minimization step and an equilibration for 340 ps, production runs were executed

for 25−1000 ns with a time step of 2 fs. In MD simulations iii, the mass density in the box during the production period for the NPT calculations varied between $\sim$1.43 and 1.49 g cm^{-3}, which is in good agreement with the experimental value of 1.489 g cm^{-3} for chloroform.

Ramachandran-type (χ_i, χ_j) histograms for MD simulations were built by using $1° \times 1°$ bins (360×360 squares). The fractional population (p_i) of each bin (χ_i, χ_j) was calculated as the number of structures in this bin divided by the total number of structures (p_N) and multiplied by 1000. The population fraction of each conformer was calculated by taking the sum of the populations in defined regions and dividing the result by the total population.

2.3. Quantum-Mechanical Calculations. All quantum mechanical calculations were carried out using Gaussian 09.[28] Geometry optimizations were carried using various combinations of QM methods and basis sets, as described in the main text. The "nosymm" keyword of Gaussian 09 was employed to carry out QM calculations with the symmetry of molecules disabled. For DFT geometry optimizations of $\mathbf{1}-\mathbf{5}$, the ultrafine numerical integration grid (with 99 radial shells and 590 angular points per shell) was used, combined with the "verytight" convergence condition (requiring the root-mean-square forces to be smaller than 1×10^{-6} hartree Bohr^{-1}). The verytight convergence condition was also employed in geometry optimizations of $\mathbf{3}$ using the MP2/6-31G(d) level of theory, as well as in HF, MP2, and CCSD calculations of $\mathbf{4}$ and $\mathbf{5}$. In the case of computationally more demanding MP2/6-31+G(d) geometry optimizations of $\mathbf{1}-\mathbf{3}$, the default convergence criterion of Gaussian 09 was used (requiring the root-mean-square forces to be smaller than 3×10^{-4} hartree Bohr^{-1}). Additional frequency calculations were also undertaken to verify that the optimized geometries correspond to true minima. NMR chemical shieldings and J couplings were computed at the B3LYP/6-311+G(2d,p) level using the gauge-including atomic orbitals (GIAO) method.[29] Chloroform solvent effects were used in all quantum mechanical calculations using the reaction field method IEFPCM (integral equation formalism of the polarizable continuum model).[30]

Conformationally averaged interatomic distances from the QM calculations were determined in a way similar to that used in NMR measurements: (i) internuclear distances (r_i) for pairs of hydrogen atoms were calculated in each conformer i; (ii) a quantity equal to r_i^{-6} was calculated as a measure of the expected NOE in each conformer, η_i; (iii) the sum of $p_i r_i^{-6}$ was used as a measure of the expected total NOE, where values of populations p_i were derived from the simulated annealing fittings of the experimentally measured $^3J_{HH}$ couplings using the QM-predicted boundary values of $^3J_{HH}$ in each conformer i; (iv) using $r = 2.40$ Å as the reference H_2—H_{3c} distance (for $\mathbf{3}$) or $r = 2.47$ Å as the reference H_{12}—H_{13} distance (for $\mathbf{1}$ and $\mathbf{2}$), internuclear distances for other proton pairs were calculated using the $\eta \sim r^{-6}$ relationship.[2a]

Natural bond orbital (NBO) analysis was carried out using NBO, version 3.1 (part of the Gaussian 09 package).[31]

3. RESULTS AND DISCUSSION

3.1. Preliminary NMR Analysis of Benzazocinones 1−3. First, we consider the analysis of experimental NMR data, focusing on NOEs and ^3J couplings of protons. In ^1H NMR spectra recorded at 298 K, the seven-spin system for the five-membered ring in $\mathbf{1}-\mathbf{3}$ showed features usually associated with

strongly coupled spin systems. A full line shape analysis[32] was therefore employed to provide accurate values of the experimental J_{HH} couplings of the aliphatic cyclic protons (Figures S1–S4 and Table S1, Supporting Information).

Single sets of peaks are observed in ^{1}H and ^{13}C NMR spectra of **1–3** in CDCl$_3$ at 298 K (Figures S1–S6, Supporting Information), suggesting that dynamic processes, including ring interconversions, occur at frequencies much greater than the chemical shift differences (in hertz) in the absence of motions, leading to averaging of the ^{1}H and ^{13}C NMR shifts, as well as the [3]J_{HH} couplings.

Low-temperature ^{1}H NMR measurements were also carried out in CDCl$_3$ and CD$_2$Cl$_2$ solutions. Two species with populations of 56% and 44% ($\pm$2%) were detected in the ^{1}H and ^{13}C spectra of amine **2** at 172 K (Figures S5 and S6, Supporting Information). As expected (and supported by MD and QM results below), these two species are associated with the change in the conformation of the eight-membered ring in **2**. No new sets of peaks were identified for **1** and **3** in the temperature range 172–333 K that could be associated with the change of the conformation of either five- or eight-membered rings.

Distances between ^{1}H nuclei (Tables S41–S43, Supporting Information) were estimated using two-dimensional NOESY spectra at 298 K. For **1** and **2**, the cross-peak due to aromatic protons H$_{12}$ and H$_{13}$ was used as a reference for determining other interproton distances. Rather than relying on H···H distances from the XRD data (which are expected to be of low accuracy),[33] we used the predicted value of 2.47 Å as the reference (H$_{12}$, H$_{13}$) distance based on the MP2/6-31+G(d) calculations (see section 3.3). In the absence of the reference (H$_{12}$, H$_{13}$) pair in amide **3**, the cross-peak due to protons H$_2$ and H$_{3c}$ was used as a reference for determining other distances. (c and t in H position numberings denote H atoms with the cis and trans configurations, respectively, relative to H$_2$.) We used 2.40 Å as the reference (H$_2$, H$_{3c}$) distance.[5]

The NOE measurements at 298 K were in favor of the C$_8$-endo conformer in amine **1**.[34] Note that the single conformer detected by NMR spectroscopy is likely to be stabilized by the remote C$_{10}$—H···N interaction (see detailed discussion in section 3.8). The NOEs between proton pairs H$_2$—H$_{8c}$ and H$_{8c}$—H$_{10}$ were in favor of the C$_8$-exo conformer in **2**, although judging by the value of the [3]J_{HH} couplings (e.g., [3]J_{8c9t} = 6.87 Hz; Table S1, Supporting Information) the presence of conformational equilibrium is likely, which results in dynamic averaging of NMR parameters. In the case of amide **3**, the observed NOEs were largely in good agreement with the single-crystal XRD structure determined at 150 K.[7]

3.2. MD Analysis of Benzazocinones 1–3. The MD stage of the combined analysis aims at identifying plausible three-dimensional geometries for a given molecule. The relative conformational populations predicted by MD are expected to be inaccurate for typical organic molecules, as the corresponding force fields and their dependence on the particular solvent environment are not verified extensively. We therefore employed three different types of MD simulations to minimize a possibility of missing a potentially plausible molecular conformation. These included (i) a GAFF[24] MD simulation with the standard pairwise generalized Born solvation model for implicit solvent simulations[25] in chloroform, (ii) an SCC-DFTB[26] MD simulation with the standard pairwise generalized Born solvation model for implicit solvent simulations[25] in chloroform, and (iii) a GAFF MD simulation with explicit solvation in chloroform.

First, we consider amide **3**, for which the X-ray structure is available. From the analysis of the distribution of endocyclic torsional angles (Figures S7–S10 in Supporting Information), the five-membered ring shows "splittings" due to the conformational heterogeneity of **3**. The MD-predicted endocyclic torsional angles of **3** are included in Table 1. All three types of simulations identified two possible conformations for the five-membered ring in **3**, referred to as major (**3a**) and minor (**3b**) conformers depending on the relative population (Table 1). No splittings were found for the endocyclic torsional angles χ_6–χ_{12}, suggesting that the conformation of the eight-membered ring is the same in both major and minor conformers. The agreement between the experimental and MD-predicted [3]J_{HH} values of **3** was estimated using the rms deviation over 18 pairs of [3]J_{HH} coupling constants (rms$_J$), which was 1.07, 1.33, and 1.06 Hz for simulations i–iii, respectively. The MD-averaged values of endocyclic torsional angles χ_1–χ_{12} in the preferred conformers from simulations i–iii showed relatively good agreement with XRD values, with mean absolute deviations of 5.5–6.4° (Table 1).

Unlike **3**, no splittings due to conformational equilibria were observed in the endocyclic torsional angle distribution curves of **1** from simulations i and iii (Figures S11–S14, Supporting Information), although the χ_1–χ_3 distributions were wider than those of χ_4–χ_{12}. In simulations ii, the broadening of the χ_1–χ_3 distributions was particularly large (Figure S12, Supporting Information). The asymmetry of these curves allows estimation of approximate values of angles χ_1–χ_3 in the less populated conformer **1b**, whereas other angles, including those of the eight-membered ring, have approximately the same values as in the major conformer **1a**. In addition, a small population of the third conformer **1c** was detected in MD simulations ii. The MD-predicted endocyclic torsional angles of **1a**–**1c** are included in Table 1. The agreement between the experimental and MD-predicted [3]J_{HH} values of **1** was estimated using the rms deviation over 20 pairs of [3]J_{HH} coupling constants (rms$_J$), which was 0.68, 1.02, and 0.70 Hz for simulations i, ii, and iii, respectively.

From the analysis of torsional distribution curves for **2**, two conformers were identified in simulations i and iii. As in the case of **3**, the minor conformer **2b** in simulations i and iii has the same geometry of the eight-membered ring as the major conformer **2a**, whereas the conformations of the five-membered rings are different in **2a** and **2b** (Table 1). Three conformers were identified in simulations ii from χ_1–χ_{12} distributions (Figures S15–S18, Supporting Information). However, considerations of Ramachandran-type (χ_i, χ_j) histograms for various combinations of χ_1–χ_{12} allowed the identification of four conformers. The (χ_4, χ_8) histogram revealing the presence of four conformations (**2a**–**2d**) in MD SCC-DFTB simulation ii is shown in Figure 1. From the two-dimensional integration of the Ramachandran-type (χ_4, χ_8) histogram, the populations of the four conformers **2d**, **2c**, **2a**, and **2b** were determined to be 72%, 21%, 5%, and 2%, respectively.

Based on the similarity of torsional angles χ_1–χ_9 (Table 1), the geometries of the first and second least populated conformers (2% and 5%) in simulation ii are the same as those of conformers **2b** and **2a**, respectively, in simulations i and iii. Judging by the values of torsional angles χ_1–χ_9 (Table 1), conformations of both the five- and eight-membered rings in the most-populated conformers **2d** (72%) and **2c** (21%) are different from those of **2a** and **2b** in simulation ii.

The conformations of the eight-membered rings are the same in **2d** and **2c** in simulations ii, whereas those of the five-membered

1096

dx.doi.org/10.1021/jp211083f | J. Phys. Chem. A 2012, 116, 1093–1109

Table 1. Endocyclic Torsional Angles[a] in Conformations Identified by MD Simulations,[b] rms Deviations of MD-Predicted $^3J_{HH}$ Couplings from the Experimental Values (rms$_J$), and Mean Absolute Deviations of 12 Endocyclic Torsional Angles (MAD$_\chi$) in the Preferred Conformer from the XRD Data for 3

conformer	method	χ_1 (deg)	χ_2 (deg)	χ_3 (deg)	χ_4 (deg)	χ_5 (deg)	χ_6 (deg)	χ_7 (deg)	χ_8 (deg)	χ_9 (deg)	χ_{10} (deg)	χ_{11} (deg)	χ_{12} (deg)	p (%)	rms$_J$ (Hz)	MAD$_\chi$ (deg)
3a	MD i	30.7	−30.7	21.8	−0.6	−17.9	−19.5	−80.6	60.9	55.7	−82.6	−6.8	29.1	93	1.07	6.4
3b		−9	25	−27	~20		c	c	c	c	c	c	c	7		
3a	MD ii	33.0	−33.3	21.6	2.4	−19.8	−27.3	−79.2	54.9	60.6	−82.2	−9.9	13.5	78	1.33	5.5
3b		−9	26	−30	~22		c	c	c	c	c	c	c	22		
3a	MD iii	30.9	−32.0	20.6	−1.4	−18.4	−18.7	−80.1	61.0	56.1	−83.0	−7.1	27.5	93	1.06	6.2
3b		−10	25	−27	~20		c	c	c	c	c	c	c	7		
3a	XRD	32.0	−40.3	32.2	−12.6	−12.1	−17.2	−87.2	55.8	60.4	−79.5	−8.1	14.6	−	−	−
1a	MD i	30.3	−5.2	−22.1	37.6	−36.9	−61.2	−52.6	65.5	44.2	−81.9	−1.3	21.5	100	0.68	
1a	MD ii	32.1	~−20	−26.0	36.0	−32.0	−61.0	−57.0	62.0	51.1	−82.0	−5.0	16.0	~53	1.02	
1b		~7	~13	~7			c	c	c	c	c	c	c	~44		
1c							−123	69	−54	99				~3		
1a	MD iii	32.1	−9.2	−17.5	38.1	−38.0	−60.0	−52.4	66.0	44.1	−81.5	−1.6	22.3	100	0.70	
2a	MD i	−25.0	5.5	19.4	−36.0	38.0	63.6	−102.0	70.8	−76.0	84.6	−0.7	−88.0	96	2.75	
2b		36	~−15	~−20	36	−39	c	c	c	c	c	c	c	4		
2d	MD ii	−6.0	25.8	−33.5	31.9	−16.6	−66.7	99.0	−62.0	−50.0	94.3	2.3	−97.0	72	2.09	
2c		29.1	−31.0	23.2	−3		c	c	c	c	c	c	c	21		
2a		−25	5.5	18	−35	36	67	−96	68	−82				5		
2b		~33		~−18	~32	~−39	c	c	c	c				2		
2a	MD iii	−25.0	5.0	20.3	−37.0	38.6	63.4	−103.0	71.6	−76.0	83.3	0.4	−88.4	97	2.75	
2b		36	~−15	~−20	35	−40	c	c	c	c	c	c	c	3		

[a] Notation of angles used (illustrated for **1**):
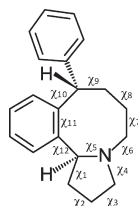
[b] (i) GAFF with implicit solvent model, (ii) SCC-DFTB with implicit solvent model, and (iii) GAFF with explicit solvent model. [c] Approximately the same as the above value.
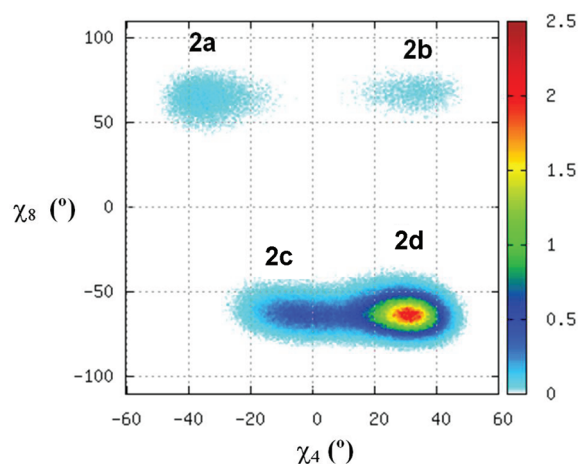

Figure 1. Ramachandran-type two-dimensional histogram revealing the presence of four conformations (**2a**−**2d**) in MD SCC-DFTB simulation ii of **2**.

rings are different. The agreement between the experimental and MD-predicted $^3J_{HH}$ values of **2** was estimated using the rms

deviation over 20 pairs of $^3J_{HH}$ coupling constants (rms$_J$), giving 2.75, 2.09, and 2.75 Hz for simulations i, ii and iii, respectively. Compared to **1** and **3**, larger values of rms$_J$ were found for **2**. Longer MD simulations (>1 μs) could, in principle, improve the accuracy of the predicted relative energies of different conformers and better reproduce the experimentally measured $^3J_{HH}$ couplings. Within the combined NMR/MD/QM approach considered here, however, the role of the MD analysis is restricted to identifying plausible molecular conformations, whereas the assessment of their relative energies rely on the joint analysis of NMR and QM data (sections 3.4 and 3.5).

3.3. Molecular Geometries from QM Analysis. At the final stage involving structure refinements by QM methods, geometry optimizations of the structures and calculations of NMR parameters by QM methods were undertaken. From the analysis of the distance (d_{C4C10} Figures S10, S14, and S18, Supporting Information) and endocyclic torsional angle distributions (Figures S7−S9, S11−S14, and S16−S18, Supporting Information), as well as χ_i/χ_j ($i \neq j$) distributions (Figure 1), different conformations of **1**−**3** were extracted from MD trajectories. In the case of **1**, 19 structures were extracted for final QM
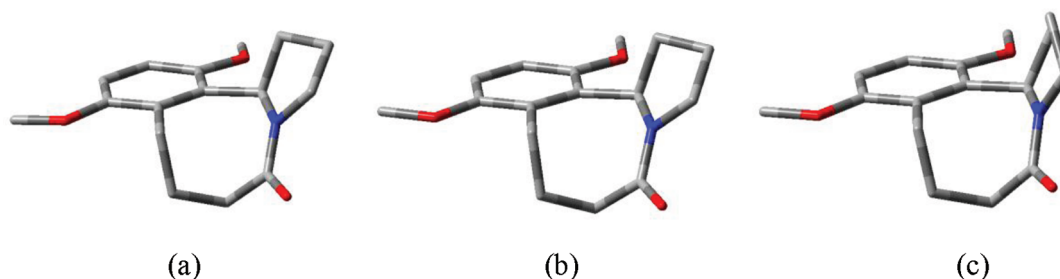
(a)

(b)

(c)

Figure 2. (a) Structure of **3** from single-crystal XRD measurements.[7] (b) Structure of major conformer **3a** from NMR/MD/QM analysis. (c) Structure of minor conformer **3b** from NMR/MD/QM analysis.

refinements (six structures from each MD simulations i and iii and seven structures from MD simulations ii). As described in section 3.8, eight additional structures of **1** were extracted from high-temperature MD simulations for QM calculations. For **3**, 18 structures were extracted for final QM refinements (six structures from each MD simulations i—iii). Because of the relatively large number of expected conformers in the case of **2** (based on NMR and MD results), 26 structures of **2** were extracted for final QM refinements (14 structures from MD simulation ii and 6 structures from each MD simulations i and iii).

*3.3.1. QM and X-ray Structures of Benzazocinone **3**.* First, we consider amide **3**, for which the X-ray structure is available. After QM geometry optimizations, the initially selected 18 structures converged into two structures, with their geometries (Tables S2—S8, Supporting Information) in agreement with those for conformers **3a** and **3b** from MD simulations (Table 1).[35] The geometry of preferred conformer **3a** from all QM calculations was similar to that determined in the solid state by XRD.[7] The final structures deduced from XRD and NMR/MD/QM analysis are shown in Figure 2.

We compared the deviations between the XRD (CCDC entry MOPHAB)[7] and various QM-predicted geometries (Table S9, Supporting Information). The lowest-energy structure was chosen for each level of theory from QM calculations. For these QM versus XRD comparisons, hydrogen atoms were excluded from consideration because of the expected low accuracy of the XRD data. In addition, aromatic CH carbons and methoxy C and O atoms, as well as the carbonyl O atom, were also excluded, leaving only non-hydrogen atoms of the five- and eight-membered aliphatic rings (Table S10, Supporting Information). For a pair of experimental (XRD) and calculated (QM) geometric parameters g^{exp} and g^{calc} (i.e., bond length, bond angle, or torsional angle), the residual is defined as $\Delta_i = g_i^{calc} - g_i^{exp}$. In line with previous work,[36] we use the mean absolute deviation [MAD = $(1/n)\Sigma_{i-1}^{n}|\Delta_i|$] and the largest residual deviation (Δ^{max}) for comparing XRD and QM geometries (Table S9, Supporting Information). From MAD values for the B3LYP,[37] M062X,[38] and MP2[39] calculations with the same split-valence double-ζ polarized basis set 6-31G(d), the M062X and MP2 calculations lead to a better agreement with the XRD data than the B3LYP calculations. In terms of largest residual deviations for bond angles and torsional angles, both M062X and MP2 show better agreement with the XRD data than B3LYP. Four different basis sets were used in the case of M062X calculations. Judging by MAD and the largest residual deviations, there is no significant difference in geometries predicted by four different basis sets, although an increase in MADs and largest deviations for torsional angles is observed on using the larger basis sets 6-31+G(d) and 6-311

+G(2d,p) compared to the smaller basis sets 6-31G(d) and 6-31G(d,p) (Table S9, Supporting Information).

In principle, the QM-calculated bond lengths approximate distances between equilibrium nuclear positions in the minimum of the potential energy surface for a motionless molecule, whereas bond lengths from XRD correspond to thermally averaged interatomic distances between the centroids of the electron density distributions at the temperature of the measurement (150 K in this case). Strictly speaking, appropriate corrections are needed to compare these two types of distances,[40] although such corrections are not straightforward.[40c] However, as is apparent from the MAD values (Table S9, Supporting Information), differences in bond lengths from QM calculations and XRD are not significant for **3**, containing only light atoms O, N, C, and H (as opposed to metal halides[40c]).

The main point of concern for our comparisons is the torsional angle, which, unlike the bond length or the bond angle, requires only small amount of energy to change its value. Comparison of X-ray and QM-predicted geometries of **3** reveals some significant differences in torsional angles (Tables S9 and S10, Supporting Information), which can, in principle, be attributed to various reasons of general nature, such as crystal packing effects and intermolecular noncovalent interactions in the solid state, as well as to the approximations made in QM calculations. The presence of large-amplitude motions (such as a ring interconversion of the five-membered ring and reorientational dynamics of the Ph and OMe groups in **3**) might also be indicative of the expected large deviations of the QM geometric parameters from the experimental results because of the flexibility of the molecular geometry. The largest deviations were observed for torsional and bond angles involving N_6-C_2 and N_6-C_7 bonds (Table S10, Supporting Information). In particular, the differences between the QM and XRD values were ~13 times larger than the estimated standard deviation for the bond angle C7—N6—C2 and ~48 times for the torsional angle C7—N6—C2—C3. On one hand, these are fragments that might be affected by the delocalization of the nitrogen lone pair and aromatic π electrons; on the other hand, intermolecular close contacts are present near these fragments (Figure 3) that could cause changes in the corresponding bond and torsional angles, thus accounting for the observed Q—X deviations (Table S10, Supporting Information). Note that the C_2—H$\cdots$O$=$C intermolecular separation is particularly close (2.38 Å, Figure 3) and is therefore expected to alter the molecular geometry in the vicinity of this intermolecular interaction in the solid state, including the bond angle $N_6-C_7-C_8$ (Table S10, Supporting Information).

As no other structural data are available for **3** in the solution or gas phase, it is difficult to single out the main reason behind the
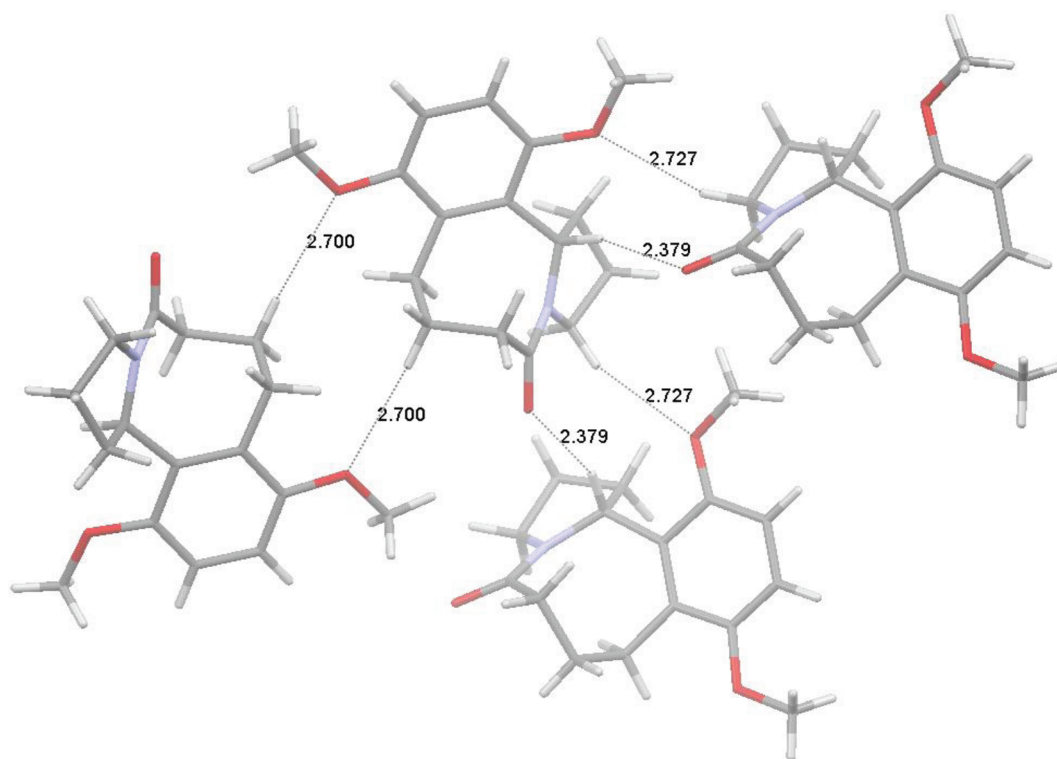
Figure 3. Arrangement of molecules in the solid state of **3** showing intermolecular C—H···O close contacts with H···O distances less than 2.8 Å for the selected molecule. Interatomic distances (in Å) are specified.

observed large differences in dihedral angles from the solid-state X-ray structure and QM calculations. Nevertheless, consideration of rigid cyclic molecules such as camphoric anhydride (**4**)[8,9] and bullvalene (**5**)[10,11] is expected to provide further insight in this regard.

*3.3.2. QM, X-ray, and Neutron Diffraction Geometries of Camphoric Anhydride **4** and Bullvalene **5**.* From comparisons of neutron diffraction data in the solid state and QM-optimized geometries of **4** (Figures S19 and S20, Tables S11—S17, Supporting Information), it is clear that relatively wider variations occur in bond lengths compared to bond angles and torsional angles. For example, B3LYP calculations predict bond lengths that are in better agreement with the neutron diffraction data than HF,[41a] M062X, MP2, and CCSD[41] calculations. Note, however, that the equilibrium bond lengths from the B3LYP calculations are usually overestimated, thus leading to fortuitously good agreement with the neutron diffraction data compared to other methods. Bond lengths between non-hydrogen atoms (Table S11, Supporting Information) from neutron diffraction measurements at 110 K (CCDC entry COQTOR01)[8] are also longer than those from XRD measurements at 110 K (CCDC entry COQTOR)[9a] and 293 K (CCDC entries FEPPARR02[9b] and FEPPAR[9c]). In fact, MADs of B3LYP/6-31G(d) versus neutron diffraction or B3LYP/6-31G(d) versus X-ray diffraction (0.011 and 0.007 Å, respectively) are smaller than that of two experimental methods X-ray diffraction versus neutron diffraction (0.017 Å).[42]

Bond angles show better agreement with the neutron diffraction data in a sequence of HF, B3LYP, M062X, and MP2 methods. In the case of CCSD calculations of **4** (as well as CCSD and MP3 calculations of **5**; Figure S21, Supporting Information), it is likely that the basis sets considered were not

sufficiently large to fully realize the potential of the method, whereas calculations with larger basis sets were prohibitively expensive. The agreement for torsional angles worsens on going from HF to B3LYP calculations, but M062X and MP2 show a comparable level of agreement with neutron diffraction, which is better than that for HF calculations. Bond angles and torsional angles obtained from neutron and X-ray diffraction measurements are in significantly better agreement than bond lengths (Figure S19, Supporting Information). Some changes in the agreement with the neutron diffraction structure occur in the case of HF and B3LYP calculations upon including hydrogen atoms into consideration, but overall, MP2 and M062X calculations show better agreement with neutron diffraction than HF and B3LYP (Figure S20 and Tables S11—S17, Supporting Information). In general, a change in the QM method causes wider variations in MAD values than a change in the basis set, in agreement with the findings for **3**.

The endocyclic torsions of **4** show some significant differences for angles χ_1, χ_2, and χ_6 (Table S12, Supporting Information). While large differences in χ_1 and χ_2 can be caused by the possible inadequacy of basis sets and QM approximations used in the presence of electronegative O atoms, the disagreement for χ_6 is somewhat surprising. Examination of the crystal structure reveals intermolecular C—H···O close contacts for the CH$_2$ groups of the χ_6 torsion (Figure 4). Similarly, the intermolecular C$_4$—H···O=C$_2$ interaction in the solid state is likely to account for the larger discrepancy in the torsional angles χ_1 and χ_2 (Figure 4). Thus, as in the case of **3**, significant QM versus XRD differences are observed in geometries of the fragments in the vicinity of intermolecular interactions in the solid state.

Remarkably, the QM-calculated endocyclic torsions show better agreement with the XRD data at 293 K than the XRD
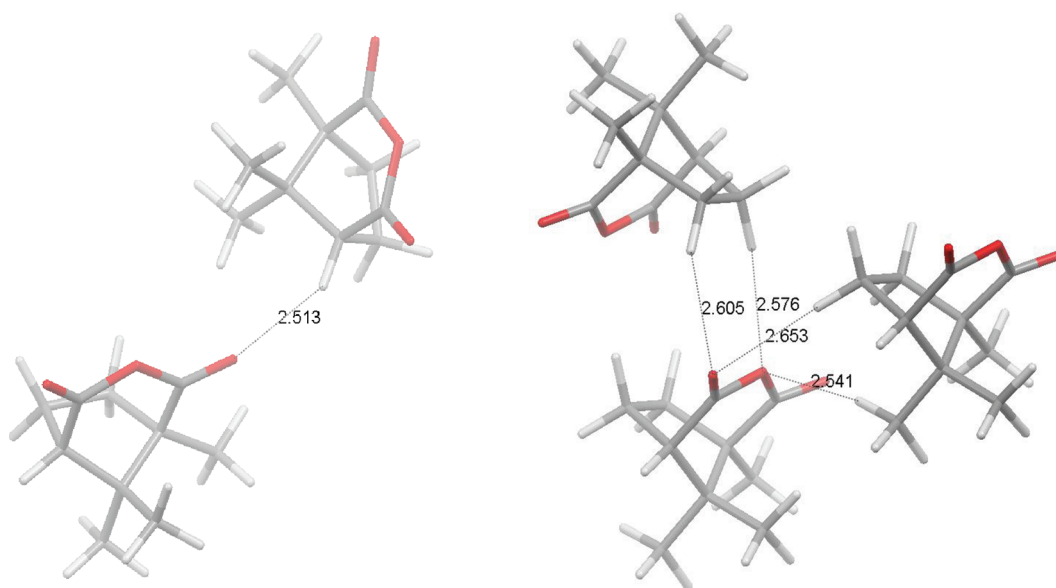
Figure 4. Arrangements of molecules in the solid state of **4** showing intermolecular C—H···O close contacts with H···O distances less than 2.8 Å for the selected molecule. Interatomic distances (in Å) are specified. Two separate views are used for clarity of presentation.
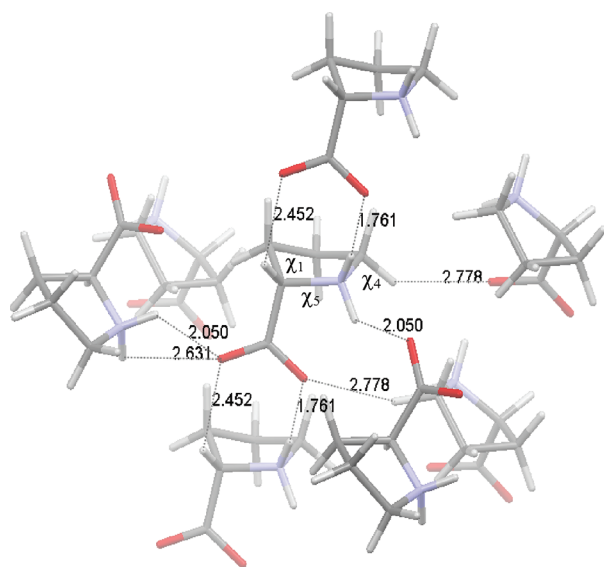

Figure 5. Arrangement of L-proline molecules in the solid state (CCDC entry PROLIN)[43] showing N^+—H···O and C—H···O close contacts with H···O distances less than 2.8 Å for the selected molecule. Interatomic distances (in Å) are specified. Labeling of torsional angles χ_1, χ_4, and χ_5 is also indicated.

and neutron diffraction data at 110 K (Tables S13 and S15—S17 Supporting Information). In principle, such a change is in agreement with the above-suggested dependence of molecular geometries on intermolecular interactions, which are likely to be more significant at lower temperatures because of the reduced amplitude and frequency of thermal vibrations.

Previously published results also suggest a significant role of intermolecular interactions in altering endocyclic torsional angles in the solid state. For example, comparison of XRD and QM data for L-proline shows significant differences in endocyclic torsional angles χ_1, χ_4, and χ_5 (8—12°, Table 6 in ref 17b),

whereas χ_2 and χ_3 show relatively small alterations (2—3°). From the XRD structure of L-proline (Figure 5),[43] there are strong intermolecular hydrogen bondings of the N^+H_2 and COO^- groups, which are expected to alter torsional angles χ_5, χ_1, and χ_4 most significantly, whereas no significant close contacts are present for the central atoms of the χ_2 and χ_3 torsions. These findings suggest that relatively large deviations of QM-predicted geometries from those measured in the solid state are caused by intermolecular noncovalent interactions. In fact, the joint analysis of the QM and solid-state molecular geometries might provide additional means for assessing the significance of intermolecular noncovalent interactions in solids.

We now compare the results for another rigid cyclic system, bullvalene **5** (Figures S21 and S22 and Tables S19—S21, Supporting Information), which, unlike **3** and **4**, does not contain electronegative atoms. Despite its symmetry, bullvalene was treated as asymmetric in QM calculations, to retain consistency of comparisons and MAD calculations as in the case of **3** and **4**. The experimental geometries from the neutron and X-ray diffraction measurements at 110 K were also asymmetric. In terms of the mean absolute deviation, the agreement between the neutron and X-ray diffraction bond lengths (Figure S21 and Table S18, Supporting Information) was ~10 times better than that for camphoric anhydride (Figure S19 and Table S11, Supporting Information).[42] Agreement for bond and torsional angles from the two diffraction techniques was also satisfactory (Figure S21, Supporting Information). The torsional MAD from the solid-state data was typically ~0.8° for M062X calculations, significantly better than that (~2°) for camphoric anhydride **4**. Similarly, the unsigned largest residual deviation in torsional angles reduces from 6.0° in camphoric anhydride to 1.9° in bullvalene. The much improved agreement for bullvalene **5** can be attributed to the fact that intermolecular interactions are relatively weak in **5** compared to **3** and **4**.

In summary, compared to **3**, MADs averaged over all the QM calculations show a ~40% improvement in the case of QM versus low-temperature XRD comparisons in **4** for torsional angles of
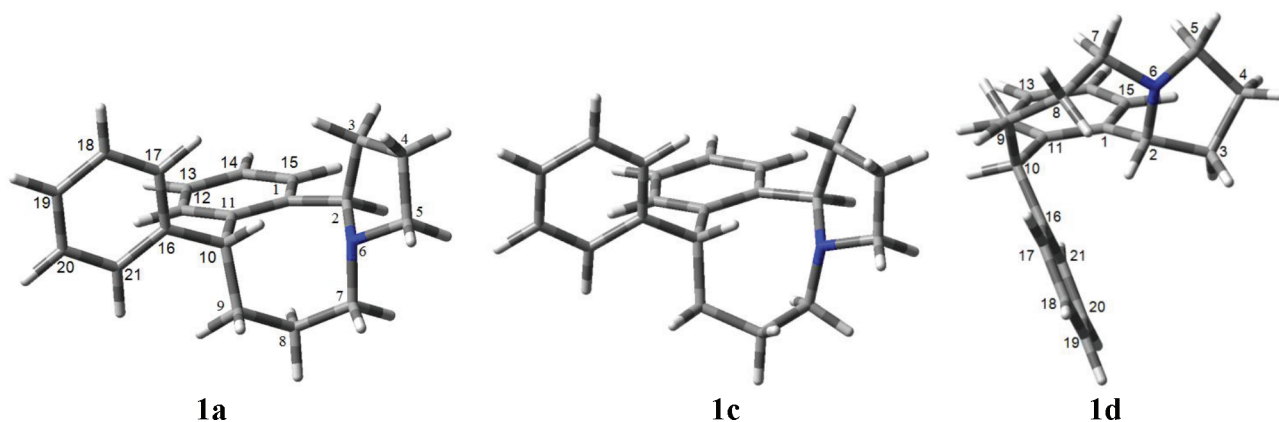
Figure 6. Structures of conformers **1a** and **1c** from NMR/MD/QM analysis, along with that of the alternative conformer **1d** (see section 3.8). Hydrogen atoms are included to illustrate the spatial proximity of proton H_{10} and the nitrogen atom (2.20 Å) in **1a** and **1c**. The distance between proton H_2 and the quaternary C atom of the Ph group (C_{16}) is 2.29 Å in **1d**.

non-hydrogen atoms (from $3.6° \pm 0.8°$ in **3** to $2.2° \pm 0.4°$ in **4**), which is significantly more rigid with only methyl hydrogens subject to large-amplitude motions. Compared to **4**, a further $\sim$70% improvement is achieved for bullvalene **5** (from $2.2° \pm 0.4°$ in **4** to $0.72° \pm 0.0.02°$ in **5**), which does not contain electronegative atoms and methyl groups.[44] Intermolecular interactions in solid **5** are expected to be relatively weak, as the shortest $C \cdots H$ intermolecular distance is 2.71 Å. For comparison, the shortest $O \cdots H$ intermolecular distances are 2.38 and 2.51 Å in **3** and **4**, respectively. Although limited in number of examples and QM methods considered, the obtained results suggest that the major differences between the solid-state structures and those from QM calculations of isolated molecules are likely to be caused by intermolecular noncovalent interactions present in the solid state, not by the deficiencies of approximations made in QM calculations.

*3.3.3. QM-Predicted Geometries of Benzazocinones **1** and **2**.* Three sets of QM calculations, namely, B3LYP/6-31G(d), M062X/6-31G(d,p), and MP2/6-31+G(d), were carried out for **1** and **2**. All three types of calculations identified two conformations **1a** and **1c** (Figure 6 and Tables S22−S24, Supporting Information). Structure **1b** identified in MD simulations ii (Table 1) converts into conformation **1a** on using QM geometry optimizations. In principle, alternative conformations of the five-membered ring in **1a** and **1c** are possible. However, the results of NMR/MD/QM analysis suggest that populations of other conformers involving the change in the five-membered ring are likely to be very low, which can be attributed to the presence of the noncovalent C_{10}—$H \cdots N$ interaction in **1a** and **1c** (Figure 6), leading to a preference for one of the conformers of the five-membered ring (see below discussion in section 3.8). From QM calculations, the relative energy of the C_8-exo conformer **1c** relative to the C_8-endo conformer **1a** was estimated to be very high: 12.6, 13.3, and 16.2 kJ mol^{-1} from B3LYP/6-31G(d), M062X/6-31G(d), and MP2/6-31+G(d), respectively, corresponding to the C8-exo populations of 0.6%, 0.5%, and 0.1%, respectively, on the assumption of a two-site exchange involving C_8-exo and C_8-endo conformers.

Three sets of QM calculations described above identified four different conformations of **2** (Figure 7 and Tables S25−S27, Supporting Information). In order of decreasing relative stability, the geometries of four conformers identified by the MP2/6-31
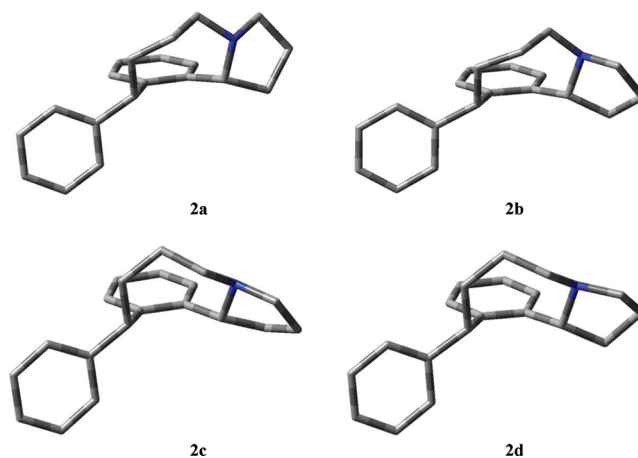

Figure 7. Structures of four conformations of **2** identified by the NMR/MD/QM analysis.

+G(d) calculations resemble those of **2d**, **2a**, **2c**, and **2b** from SCC-DFTB MD calculations ii (Table 1), although there are significant differences in the geometries of the five-membered rings. It is noteworthy that M062X/6-31G(d,p) and B3LYP/6-31G(d) predict stabilities of conformers in the order **2a** > **2d** > **2b** > **2c** and **2d** > **2b** > **2c** > **2a**, respectively, which disagree with that predicted by the MP2/6-31+G(d) calculations (**2d** > **2a** > **2c** > **2b**). At the same time, the geometries of the four conformers predicted by three sets of QM calculations show good agreement among each other (Tables S25−S27, Supporting Information).

3.4. Conformer Populations of Amide 3 from the Analysis of Vicinal Coupling Constants. The conformational exchange between **3a** and **3b** involves interconversion of the five-membered ring. NMR measurements at temperatures as low as 172 K were not sufficient to freeze the expected exchange process between **3a** and **3b**. In principle, the results of QM calculations can be used to estimate populations of conformers. However, despite their satisfactory accuracy in predicting molecular geometries, the performance of QM methods in predicting energetic characteristics such as relative stabilities of conformers is not always satisfactory.[38,45−47] Populations of conformers **3a** and **3b** determined from the relative free energies of conformers predicted by QM calculations are included in Table S9

Table 2. Population p_{3a} of Conformer 3a from Fittings of Experimental $^3J_{HH}$ Couplings Using a Two-Site Exchange Model[a] and the B3LYP/6-311+(2d,p)-Calculated NMR J Couplings in 3a and 3b as Boundary Values

geometry optimization[b]	p_{3a} (%)	rms$_J$[c] (Hz)
B3LYP/6-31G(d)	83.9	0.75
M062X/6-31G(d)	83.6	0.79
M062X/6-31G(d,p)	83.7	0.81
M062X/6-31+G(d)	83.5	0.78
M062X/6-311+G(2d,p)	83.7	0.82
MP2/6-31G(d)	83.5	0.78
MP2/6-31+G(d)	83.3	0.81

[a] 3a $\rightleftharpoons$ 3b, with $p_{3b} = 100 - p_{3a}$. [b] QM level of theory used to optimize the geometries for the B3LYP/6-311+(2d,p) calculations of NMR J couplings. [c] rms deviation of the conformationally averaged $^3J_{HH}$ couplings from the experimental values.

(Supporting Information). Although conformer **3a** is predicted to have a higher population than conformer **3b** in all cases, values of p_{3a} vary over a relatively wide range (67–88%).

As the conformational change between **3a** and **3b** involves interconversion of the five-membered ring, the experimental value of p_{3a} = 80.9% was estimated using simulated annealing fittings of 10 $^3J_{HH}$ couplings of the five-membered ring (with the least-squares fitting error of ±0.5%).[17b] From these results, M062X calculations reproduce the relative energies of two conformers of **3** better than other QM methods considered (Table S9, Supporting Information). However, simulated annealing fittings of $^3J_{HH}$ couplings rely on the accuracy of the empirically optimized Karplus-type relationships.[14] We therefore considered an alternative hybrid approach combining experimental and calculated NMR J couplings using QM methods (Tables S28–S40, Supporting Information) to derive populations of conformers.

The hybrid method for determining populations of conformers relies on the assumption that QM methods reproduce experimentally measured molecular geometries and NMR J couplings with satisfactory accuracy. The QM-optimized geometries of the lowest-energy conformers **3a** and **3b** were used in calculations of 18 $^3J_{HH}$ couplings ($^3J_i^{3a}$ and $^3J_i^{3b}$, where i = 1, 2, ..., 18) at the B3LYP/6-311+G(2d,p) level of theory (Tables S34–S40, Supporting Information), which reproduces the experimental J couplings well.[17b] As in the case of geometry optimizations, the IEFPCM method was used in NMR calculations to account for solvation effects in chloroform. The calculated NMR couplings $^3J_i^{3a}$ and $^3J_i^{3b}$ were then used as boundary values in fittings of experimentally measured $^3J_{HH}$ values of **3** ($^3J_i^{exp}$) on the assumption of a two-site exchange model

$$\langle {}^3J_i^{calc}\rangle = [p_{3a}{}^3J_i^{3a} + (100 - p_{3a}){}^3J_i^{3b}]/100$$

where p_{3a} is the population of conformer **3a** (in percent). The rms deviation of $^3J_i^{calc}$ from $^3J_i^{exp}$ was then minimized using simulated annealing fittings, in which the value of p_{3a} was optimized. The results of the fittings are summarized in Table 2. The value of p_{3a} varies between 83.3% and 83.9% and is in agreement with the value of 80.9% obtained from fittings of $^3J_{HH}$ couplings of the five-membered ring relying on Karplus equations of Haasnoot et al., without the use of the QM data. The rms$_J$ deviation for QM-optimized geometries using seven different levels of theory varies between 0.75 and 0.82 Hz, which falls into a typical range of deviation from experiment for NMR J coupling

Table 3. Populations of Conformers of 2 from Fittings of Experimental $^3J_{HH}$ Couplings Using a Four-Site Exchange Model and the B3LYP/6-311+(2d,p)-Calculated NMR J Couplings in Four Conformers of 2 as Boundary Values

geometry optimization[a]	p_{2d} (%)	p_{2c} (%)	p_{2a} (%)	p_{2b} (%)	rms$_J$[b] (Hz)
B3LYP/6-31G(d)	35.8	24.8	15.2	24.2	0.82
M062X/6-31G(d,p)	33.2	26.7	17.4	22.7	0.79
MP2/6-31+G(d)	33.0	29.4	21.1	16.5	0.70

[a] QM level of theory used to optimize the geometries for the B3LYP/6-311+(2d,p) calculations of NMR J couplings. [b] rms deviation of the conformationally averaged $^3J_{HH}$ couplings from the experimental values.

predictions at the B3LYP/6-311+G(2d,p) level.[17b] We note that the value of rms$_J$, as well as values of rms deviations for internuclear distances (section 3.6) and chemical shifts (section 3.7), can be considered as a quality indicator of the reliability of structures predicted by the NMR/MD/QM approach.

3.5. Conformer Populations of Amines 1 and 2 from the Analysis of Vicinal Coupling Constants. As in the case of **3**, the QM-optimized geometries of the lowest-energy conformers of **1** and **2** were used in calculations of J couplings at the B3LYP/6-311+G(2d,p) level of theory (Tables S28–S33, Supporting Information). Compared to the experimental $^3J_{HH}$ couplings, the calculated values of 20 $^3J_{HH}$ couplings for a single predominant conformer **1a** showed the rms$_J$ deviations of 0.85, 0.86, and 0.83 Hz for molecular geometries optimized at the B3LYP/6-31G(d), M062X/6-31G(d,p), and MP2/6-31+G(d) levels of theory, respectively. The C8-exo conformer **1c** showed the rms$_J$ deviations of 4.04, 4.04, and 4.03 Hz for molecular geometries optimized at the B3LYP/6-31G(d), M062X/6-31G(d,p), and MP2/6-31+G(d) levels of theory, respectively. Assuming a two-site exchange model between **1a** and **1c**, the hybrid approach described above predicts 0% population of **1c** [compare to 0.6%, 0.5%, and 0.1% as predicted by B3LYP/6-31G(d), M062X/6-31G(d) and MP2/6-31+G(d), respectively]. Thus, we considered only the C8-endo conformer **1a** in our further analysis of NMR parameters.

The rms$_J$ values for each of four conformations of **2** on using the MP2/6-31+G(d)-optimized geometries were 2.61 Hz (**2d**), 2.59 Hz (**2c**), 3.00 Hz (**2a**), and 2.23 Hz (**2b**), suggesting that a conformational exchange model needs to be considered to fit experimental $^3J_{HH}$ couplings. Upon using the hybrid approach relying on both experimental and calculated NMR data, the rms$_J$ value reduced to 0.70 Hz on the assumption of a four-site exchange model for **2** with the following populations of conformers at 298 K: 33% **2d**, 29% **2c**, 21% **2a**, and 16% **2b** (Table 3). The experimentally measured values of 56% and 44% (±2%) at 172 K reflect the populations of the eight-membered ring and can be compared to the sum of populations $p_{2d} + p_{2c}$ (62%) and $p_{2a} + p_{2b}$ (38%) predicted by the hybrid approach at 298 K, as the interconversion of the five-membered ring is likely to be fast on the NMR time scale at 172 K and the conformation of the eight-membered ring is the same within each pair of conformations **2d/2c** and **2a/2b** (Figure 7).

3.6. Experimental and Calculated NOEs for Benzazocinones 1–3. The populations of conformers obtained from the analysis of $^3J_{HH}$ couplings also agree well with measured NOEs from two-dimensional NOESY spectra. In particular, the interatomic distances (r_i^{calc}, Å) extracted from the MP2/6-31+G(d)-optimized geometry of the predominant conformer **1a** show the rms deviation (rms$_d$) of 0.077 Å for 20 pairs of protons,

Table 4. Experimental and Calculated ^{1}H and ^{13}C Chemical Shifts in 1 (δ)^a and rms (rms$_\delta$) and Largest Residual (Δ_δ^{max}) Deviations between the Calculated and Experimental Values

proton	δ_H^{exp} (ppm)	$\delta_H^{*calc\ b}$ (ppm)	$\delta_H^{calc\ c}$ (ppm)	carbon	δ_C^{exp} (ppm)	$\delta_C^{*calc\ b}$ (ppm)	$\delta_C^{calc\ c}$ (ppm)
2	3.47	3.67	3.49	1	142.7	148.4	144.1
3c	2.22	2.32	2.20	2	71.1	74.6	72.5
3t	1.88	2.04	1.94	3	37.4	39.1	37.9
4c	1.76	1.83	1.74	4	22.2	22.1	21.5
4t	1.91	2.08	1.97	5	56.3	57.9	56.2
5c	2.19	2.37	2.25	7	55.7	56.5	54.9
5t	3.12	3.24	3.08	8	24.4	25.8	25.0
7c	2.53	2.67	2.54	9	33.1	34.2	33.2
7t	3.03	3.21	3.06	10	43.3	45.3	44.0
8c	1.47	1.53	1.46	11	142.2	149.8	145.4
8t	1.55	1.60	1.52	12	129.1	132.6	128.8
9c	1.93	2.08	1.98	13	126.4	128.5	124.8
9t	2.13	2.08	1.98	14	125.2	127.3	123.6
10	6.47	6.97	6.63	15	127.4	130.1	126.4
12	6.60	6.78	6.45	q-Ph	145.5	152.0	147.6
13	7.00	7.33	6.97	o-Ph	128.9	131.8	128.0
14	7.07	7.39	7.03	m-Ph	128.1	130.6	126.8
15	7.09	7.49	7.12	p-Ph	125.7	127.9	124.2
o-Ph	7.32	7.73	7.35				
m-Ph	7.34	7.74	7.35				
p-Ph	7.23	7.61	7.23				
rms$_\delta$	−	0.25	0.07	rms$_\delta$	−	3.4	1.3
Δ_δ^{max}	−	0.50	0.16	Δ_δ^{max}	−	7.6	3.2

^{a} Optimized geometries of **1a** from B3LYP/6-31G(d) IEFPCM(CHCl$_3$) were used in GIAO B3LYP/6-311+G(2d,p) IEFPCM(CHCl$_3$) chemical shift calculations. ^{b} Calculated isotropic shieldings (σ^{calc}) were subtracted from the intercept [$b(^1$H$) = 31.92$ ppm and $b(^{13}$C$) = 179.77$ ppm] of the plot of the calculated isotropic shielding against the experimental chemical shift values (δ^{exp}) to convert these values into calculated chemical shifts ($\delta^{*calc} = b - \sigma^{calc}$). ^{c} Calculated chemical shifts [$\delta^{calc} = (\sigma^{calc} - b)/a$] were determined using the slope [$a(^1$H$) = -1.05$ and $a(^{13}$C$) = -1.03$] and the intercept [$b(^1$H$) = 31.92$ ppm and $b(^{13}$C$) = 179.77$ ppm] derived from the least-squares fittings [$\sigma^{calc}(i) = a\delta^{exp}(i) + b$]. All inequivalent ^{1}H ($N = 21$) and ^{13}C ($N = 18$) sites listed were included in the least-squares fittings.

for which experimental data are available (r_i^{exp}, Å; Table S41, Supporting Information). The corresponding rms$_d$ values for B3LYP/6-31G(d) and M062X/6-31G(d,p) geometries of **1a** were 0.073 and 0.070 Å, respectively (Table S41, Supporting Information).

For benzazocinone **2**, we extracted interatomic distances from MP2/6-31+G(d)-optimized geometries of **2d**, **2c**, **2a**, and **2b** for 18 pairs of protons (Table S42, Supporting Information). The rms deviations of r_i^{calc} from r_i^{exp} (rms$_d$) were 0.48 Å (**2d**), 0.64 Å (**2c**), 0.59 Å (**2a**), and 0.67 Å (**2b**) for the individual conformers, whereas averaging of the calculated NOEs over the four conformations (with the populations shown in Table 3) lead to the rms$_d$ value of 0.11 Å. Similar improvements were also obtained for other QM calculations considered (Table S42, Supporting Information). Here, the assumption of fast-exchange averaging for the analysis of NOEs is based on the fact that dynamic processes that are fast on the NMR chemical shift time scale are also fast relative to the ^{1}H spin−lattice relaxation rates, as typical ^{1}H spin−lattice relaxation times for small organic molecules in the solution state are on the order of seconds (for a detailed discussion, see section 5.3 of ref 2a).

For the two identified conformers of **3** with populations of 83% (**3a**) and 17% (**3b**) [MP2/6-31+G(d), Table 2], the rms$_d$ values are 0.12 and 0.52 Å, respectively. On averaging over two conformations, the calculated NOEs lead to the rms$_d$ value of 0.11 Å (Table S43, Supporting Information). Similar improvements

were also obtained for other QM calculations considered (Table S43, Supporting Information).

3.7. Experimental and Calculated Chemical Shifts of Benzazocinones 1−3. As a third NMR parameter for structure and relative stability verifications, we used chemical shifts. Compared to ^3J couplings and NOEs, NMR chemical shifts exhibit a more complex structural and electronic dependence.[3,13,32b,48] In principle, QM calculations are ideally suited for predicting chemical shifts. In practice, however, a posteriori corrections are often needed to assist comparisons of experimental and calculated chemical shifts.[49]

In Table 4, we compare experimental and calculated chemical shifts of **1**. As shown previously,[49b,e] instead of separate calculations of the isotropic chemical shielding in the reference compound [e.g., tetramethylsilane (TMS) for ^{1}H, ^{13}C, and ^{29}Si NMR spectroscopy], one can plot the calculated isotropic shieldings (σ^{calc}) against the experimental chemical shift values (δ^{exp}) and subtract the calculated shieldings from the intercept (b) of the resulting regression to convert them into chemical shifts: $\delta^{calc} = b - \sigma^{calc}$ (shown as δ_H^{*calc} and δ_C^{*calc} in Table 4 for ^{1}H and ^{13}C chemical shifts of **1**). This approach is expected to compensate for systematic errors of the method and does not depend on the accurate calculation of the reference molecule (TMS). The use of both the slope and intercept of the σ^{calc} versus δ^{exp} plot for chemical shift conversion [$\delta^{calc} = (\sigma^{calc} - b)/a$] has also been reported[3a,49b,49d,49e] (shown as δ_H^{calc} and δ_C^{calc} in Table 4 for

^{1}H and ^{13}C chemical shifts of **1**). As illustrated for the single predominant conformer **1a** of **1**, the use of both the slope and the intercept of the σ^{calc} versus δ^{exp} plot for chemical shift conversions leads to a significantly improved agreement with the experimental data (rms$_{\delta H}$ = 0.07 ppm and $\Delta_{\delta H}^{max}$ = 0.16 ppm; rms$_{\delta C}$= 1.3 ppm and $\Delta_{\delta C}^{max}$ = 3.2 ppm) compared to the referencing relative to TMS only (Table 4). Performance improvements of similar magnitude were also obtained by using optimized geometries of **1a** from M062X/6-31G(d,p) and MP2/6-31+G(d) calculations (Tables S44 and S45, Supporting Information). We therefore used both the slope and the intercept of the δ^{calc} versus δ^{exp} dependence for determining values of calculated chemical shifts in the remainder of this work [i.e., $\delta^{calc} = (\sigma^{calc} - b)/a$].

We now consider a more general case, in which conformational heterogeneity is taken into account. Optimized geometries of four lowest-energy conformers of **2** (**2a**–**2d**) and the two lowest-energy conformers of **3** (**3a** and **3b**) were used in GIAO B3LYP/6-311+G(2d,p) chemical shielding calculations. The conformationally averaged values of the isotropic shieldings were calculated as

$$\langle \sigma^{calc}(i) \rangle = \sum_{j=1}^{M} p_j \sigma_j^{calc}(i)$$

where $\langle \sigma^{calc}(i) \rangle$ is the conformationally averaged value of the isotropic shielding of proton i, M is the number of conformations, p_j is the population of conformation j (Tables 2 and 3), and $\sigma_j^{calc}(i)$ is the calculated isotropic shielding of the proton i in conformation j. The average values of the isotropic shieldings were then converted into conformationally averaged values of chemical shifts [$\langle \delta^{calc}(i) \rangle$] using both the slope and the intercept of the σ^{calc} versus δ^{exp} plot, as described above. From the results obtained (Tables S44–S55, Supporting Information), the rms$_\delta$ values for **1**–**3** varied in the ranges 0.05–0.08 ppm (^{1}H) and 1.0–2.1 ppm (^{13}C).

3.8. Noncovalent C—H···N Interaction in Benzazocinone 1.
In recent years, there has been renewed interest in weak noncovalent interactions in condensed phases,[50] primarily driven by the importance of these interactions in biomedical and supramolecular materials.[50,51] In many cases, weak noncovalent interactions are first characterized in the solid state, where favorable conditions exist for their detection due to "motionless" molecules in solids.[50c,e,i,52] Whereas translational motions of molecules are indeed mostly absent in the solid state, reorientational motions (of either a molecule as a whole or a particular fragment in a molecule) are often not suppressed, and their presence might be dependent on the strength of intermolecular noncovalent interactions. The existence of intermolecular noncovalent interactions between solute molecules in the solution state is less likely than in the solid state, as the solvent–solute interactions, as well as translational and reorientational dynamics of molecules, lead to a breakdown of interactions between the solute molecules, although self-association effects as a consequence of noncovalent binding can become important at low temperatures or high concentrations.[53] Another factor that favors the detection of noncovalent interactions in solids is that reliable diffraction techniques exist for structure determinations in the solid state, whereas the interpretation of spectroscopic parameters measured in solutions is not straightforward. Weak noncovalent C—H···O and C—H···N interactions are representative in this regard. For instance, based on a survey of 113

published neutron diffraction crystal structures, it was concluded that hydrogen atoms covalently bonded to carbon have a statistically significant tendency to form short intermolecular contacts to oxygen atoms, which was attributed to electrostatic stabilization of the short C—H···O contacts.[54] The crystal structures also showed several short C—H···N contacts. However, the detected short C—H···N contacts were intermolecular. One recent example include identification of C(sp^3)—H···N≡C in the solid state.[55] Regarding the solution phase, there are few reports describing C—H···N interactions, and the detected short C—H···N contacts involve either sp^2- or sp-hybridized nitrogen atoms.[56] Theoretical studies of C(sp^3)—H···N(sp^3) are also limited. Gas-phase ab initio calculations for the methane–ammonia complex have been reported, where the bond dissociation energy for the C—H···N hydrogen bond was estimated to be 2.5 kJ mol^{-1}.[57]

Here, we examined "chemical shift–structure" relationships available from experiment and QM calculations to reveal the reason behind the high-frequency shift of one of the protons (Table 4; Tables S44 and S45 in Supporting Information). In particular, the H$_{10}$ proton in **1** resonates at the unusually high frequency of δ_H = 6.47 ppm for aliphatic protons. From GIAO B3LYP/6-311+G(2d,p) NMR calculations of the predominant conformer **1a** (Figure 6) using geometries optimized at three different levels of theory, the chemical shift of proton H$_{10}$ was predicted to be 6.58–6.68 ppm, which reproduces the experimentally observed high-frequency shift of 6.47 ppm for **1a** measured in CDCl$_3$ at 298 K. Consideration of model molecules in which aromatic rings were removed from the structures of **1** and **2** confirmed that the observed high-frequency shift of proton H$_{10}$ is likely to be caused by the C—H···N interaction (Figure S23, Supporting Information).

To estimate the role of the C—H···N interaction in **1a**, we considered a theoretically plausible conformer in which the eight-membered ring has inverted with the loss of the C—H···N interaction. To increase the populations of less populated conformers at ambient temperatures, we carried out additional SCC-DFTB MD simulations ii at 500 and 1000 K. The increase of temperature allowed us to identify new conformers. Figure 8 compares distributions of the N···H$_{10}$ distance and the endocyclic torsional angle χ_6 in variable-temperature MD simulations ii at 300 K (125 ns), 500 K (25 ns), and 1000 K (25 ns). Remarkably, the population of the conformer with the N···H$_{10}$ distance of ~4.6 Å increases from 0% in MD simulation ii at 300 K to 37% in MD simulation ii at 1000 K. Furthermore, whereas conformer **1c** (with $\chi_6 \approx -123°$) appears only after 88 ns of MD simulations at 300 K, it can be detected in MD simulations within the first 1 ns of simulation at 1000 K and 2.5 ns at 500 K. These preliminary results suggest that short high-temperature MD simulations can be employed successfully for the identification of possible molecular geometries, which could prove particularly useful in MD simulations relying on QM treatments. Several different structures were selected from the MD simulations ii at 1000 K with the N···H$_{10}$ distance varying between 4.35 and 5.04 Å (Figure 8a) and with the endocyclic torsional angle varying between $\chi_6 \approx -123°$ and $\chi_6 \approx 67°$ (Figure 8b) for QM geometry optimizations to estimate relative stabilities of additional conformers predicted by the high-temperature MD simulations. The energy of the four unique conformers relative to that of **1a** [$\Delta G(298K)$] were 14.8, 21.3, 21.4, 33.1, and 33.9 kJ mol^{-1} on using M062X/6-31G(d) IEFPCM-(CHCl$_3$) calculations. We therefore used only the lowest-energy
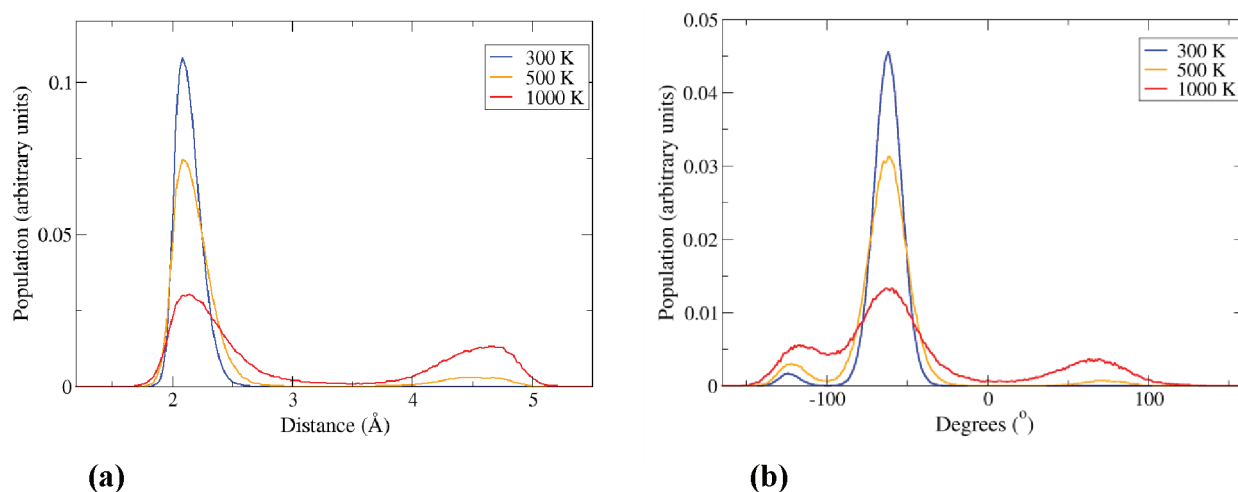
1104

dx.doi.org/10.1021/jp211083f |*J. Phys. Chem. A* 2012, 116, 1093–1109

Figure 8. Distributions of (a) the interatomic distance between atoms N and H_{10} and (b) the endocyclic torsional angle χ_6 from variable-temperature SCC-DFTB MD simulations ii of **1** at 300 K (125 ns, blue), 500 K (25 ns, orange), and 1000 K (25 ns, red).

Table 5. Geometric Characteristics of C_{10}—H$\cdots$N and C_2—H$\cdots$C$_q$[a] Close Contacts in 1a and 1d, Respectively, from QM Calculations

	C_{10}—H distance (Å)	$H_{10}\cdots$N distance (Å)	$C_{10}\cdots$N distance (Å)	C_{10}—H$\cdots$N angle (deg)	C_2—H distance (Å)	$H_2\cdots C_q$ distance (Å)	C_2—H$\cdots C_q$ angle (deg)
			MP2/6-31+G(d)				
1a	1.0930	2.1966	2.8503	116.0	1.1141		
1d	1.1024				1.0922	2.2900	132.5
			M062X/6-31G(d,p)				
1a	1.0911	2.2226	2.8667	115.5	1.1103		
1d	1.0987				1.0912	2.3494	132.6
			B3LYP/6-31G(d)				
1a	1.0912	2.2239	2.8965	117.7	1.1102		
1d	1.0998				1.0908	2.4072	133.9

[a] C_q represents the quaternary C atom of the C_6H_5 group.

conformer from the new set of QM calculations in our further analysis (denoted as **1d**, Figure 6).

From the MP2/6-31+G(d) geometry optimizations, the distance between the N atom and the H_{10} proton is 2.197 Å in **1a** (Table 5), suggesting that the significant high-frequency shift of H_{10} in **1a** is induced by the proximity of this proton to the lone pair (LP) of the N atom. It is likely that the C—H$\cdots$LP—N noncovalent interaction acts as a weak stabilizing factor in the major conformer **1a**. When compared to conformer **1d** with no C_{10}—H$\cdots$N interaction, the C_{10}—H bond in **1a** was found to shrink by ∼0.7%. (Table 5). A similar C—H bond contraction was previously reported for C—H$\cdots\pi$ interactions.[24] Interestingly, the distance between proton H_2 and the quaternary C atom (C_q) of the Ph group is 2.29 Å in **1d**, which indicates the possible presence of a C_2—H$\cdots\pi$(Ph) interaction in **1d** (Figure 6).

A natural bond orbital (NBO) analysis was carried out at the M062X/6-31G(d,p) level using geometries optimized at the same level of theory (Table S56, Supporting Information). As there is no C_{10}—H$\cdots$N close contact in **1d**, the changes in the parameters of **1a** relative to the parameters of **1d** were used for the assessment of the C_{10}—H$\cdots$N interaction in **1a**. Similarly, there is no C_2—H$\cdots\pi$(Ph) close contact in **1a**, which

allowed us to use the changes in the parameters of **1d** relative to parameters of **1a** to assess the significance of the C_2—H$\cdots\pi$(Ph) interaction in **1d**.

In both cases, the corresponding C—H bonds contract in the presence of noncovalent remote interactions (Table 5). The X—H bond shortening in the X—H$\cdots$Y hydrogen-bonding unit is indicative of a blue shift of the X—H IR stretching frequency, and the corresponding X—H$\cdots$Y interaction is referred to as an "improper" or "blue-shifted" hydrogen bond.[58,59] The calculated harmonic C_{10}—H stretch vibration frequency is blue-shifted by 92 cm^{-1} in **1a** compared to **1d**, and the C_2—H stretch vibration frequency is blue-shifted by 227 cm^{-1} in **1d** compared to **1a**.

From the natural atomic orbital analysis, the occupancy of H_2 and H_{10} atoms decreases in the presence of close contacts (Table S56, Supporting Information). The H atoms subjected to close contacts become more electropositive. The NBO analysis revealed that, in the presence of noncovalent interactions [either the C_{10}—H$\cdots$N interaction in **1a** or the C_2—H$\cdots\pi$(Ph) interaction in **1d**], the s character of the corresponding C—H bond increases by approximately 2%. Expressed as a percentage, the relative increase in the s character seems insignificant, whereas expressed as the ratio of s to p electrons in a given

hybrid orbital, the change is significant: from $sp^{3.85}$ in **1d** to $sp^{3.42}$ in **1a** for the C_{10}—H bond and from $sp^{3.29}$ in **1d** to $sp^{2.97}$ in **1a** for the C_2—H bond.

The second-order perturbation theory analysis of the Fock matrix in the NBO basis, which is used to estimate the energies of delocalization of electrons from filled NBOs into empty NBOs, showed (i) $n_N \rightarrow \sigma^*(C_{10}$—H) delocalization from the nitrogen lone pair into the C_{10}—H antibond with a stabilization energy of 2.89 kcal mol^{-1} in **1a** and (ii) $\sigma(C_{10}$—H) $\rightarrow n^*_N$ delocalization from the C_{10}—H bond into the empty Rydberg orbital of the nitrogen lone pair with a stabilization energy of 0.57 kcal mol^{-1} in **1a**. The stabilization energies for these delocalizations between C_{10}—H and the nitrogen lone pair were less than 0.5 kcal mol^{-1} in **1d**. The $n_N \rightarrow \sigma^*(C_{10}$—H) delocalization found in **1a** is known as hyperconjugative charge transfer from the lone pair of a heteroatom to the $\sigma^*(C$—H) orbital.[59] Both the delocalization of electrons into the C—H antibond and their delocalization from the C—H bond are expected to elongate the C—H bond. However, as shown previously, hyperconjugation with a stabilization energy below the 3−5 kcal mol^{-1} threshold can be considered as weak.[59b] According to the model developed by Alabugin et al.,[59b] the overall bond length change is determined by the balance of hyperconjugation and rehybridization. Under this model, the C—H bond contraction in the C_{10}—H···N noncovalent bonding in **1a** can be attributed to the increase of the s character of the C—H bond, which, in turn, is caused by the electron density decrease on the hydrogen atom placed in the vicinity of the nitrogen lone pair.

4. CONCLUDING REMARKS

We have explored the potential of a combined NMR/MD/ QM approach as a universally applicable technique for full structure and dynamics characterizations in solutions. Experimental and QM-predicted values of three different parameters, namely, J couplings, chemical shifts, and interproton distances, were used for comprehensive verifications of structures derived from the MD/QM analysis. The rms deviation of the calculated values from the experimental values was used as the merit function in the combined analysis and varied in the ranges 0.7−0.9 Hz for $^3J_{HH}$ couplings, 0.05−0.08 ppm for ^1H chemical shifts, 1.0−2.1 ppm for ^{13}C chemical shifts, and 0.07−0.11 Å for interproton distances. These values of rms deviations serve as initial estimates of quality thresholds for structure verifications in solution using NMR/MD/QM analysis. There is further possibility for reducing these thresholds, for example, by identifying more accurate QM methods for predicting NMR parameters or by employing linear scaling factors not only for QM-predicted chemical shifts but also for NMR J couplings.[4h,60] When necessary, the number of experimental parameters can also be increased further using geminal and long-range J_{HH} couplings, as well as J couplings for ^{13}C—^1H pairs or other nuclei.[5,6n]

In terms of the chemical significance of the results provided by the combined approach, the geometry of the preferred conformer of benzazocinone **3** from the NMR/MD/QM analysis is similar to that from the single-crystal X-ray diffraction. The NMR/MD/QM approach also allows the identification and full characterizion of the second (less populated) conformation of **3** in the solution state, which was otherwise unknown. The potential of the NMD/MD/QM analysis is further demonstrated using benzazocinone **1**, showing a single dominant conformer, and its isomer **2**, showing four interexchanging conformers, for

which no X-ray data are available, as these are not solids. A unique example of $C(sp^3)$—H···$N(sp^3)$ intramolecular noncovalent interaction in **1** was also detected and characterized using the NMR/MD/QM and NBO analyses. Overall, the results suggest that, in the case of typical cyclic organic molecules where only a few possible conformations exist, the performance of the MD force field or the semiempirical Hamiltonian is not critical and the final geometry refinements of the structures selected from the MD simulations using QM methods are sufficient for correcting for the expected inaccuracy of the MD analysis.

As the NMR/MD/QM analysis relies heavily on the final QM geometry optimization, particular attention was paid to comparisons of geometric characteristics predicted by different QM methods and those from X-ray and neutron diffraction measurements. The choice of the diffraction-based structures in the solid state is forced rather than justified, as there are no experimentally determined structures in solution. Although the QM-predicted geometries of **3** showed overall good agreement with that in the solid state, significant differences were found for some of the torsional angles. To assess whether the possible source of discrepancy is due to ring dynamics in **3**, conformationally rigid camphoric anhydride **4** and bullvalene **5** were used to examine various combinations of QM methods and basis sets. Despite the limited number of examples and QM methods considered, the comparative analysis of structures suggests that the major differences between the solid-state structures and those from QM calculations of isolated molecules are caused by intermolecular noncovalent interactions present in the solid state, not by the deficiencies of approximations made in QM calculations. Rather speculatively, one can assume that the energy released upon formation of intermolecular noncovalent bondings during the crystallization process is absorbed by nearby atoms of the solute, leading to low-energy intramolecular structure alterations wherever possible. The stronger the noncovalent interaction, the higher the energy emitted, thus the larger the expected structural alterations. Relatively strong noncovalent interactions or combinations of several noncovalent interactions can also cause longrange alterations of intramolecular geometries.[12] We note that the significance of intermolecular interactions in altering preferred intramolecular geometries of isolated molecules was considered before,[33c] with the recent report focusing on the quantification aspects of this effect.[61]

Taking into consideration the values of the largest residuals for **3** and **4** showing significant intermolecular interactions in the solid state, the QM-predicted geometric parameters by HF, B3LYP, M062X, and MP2 calculations were within the following limits of the parameters in the solid state: ±0.07 Å (bond lengths), ±3° (bond angles), and ±10° (torsional angles). From mean absolute deviations, the corresponding limits of agreement are within ±0.03 Å for bond lengths, ±0.8° for bond angles, and ±3.2° for torsional angles. Even though comparable in reproducing geometric characteristics, MP2 calculations with mainly Dunning's correlation-consistent basis sets [cc-pVDZ-aug(O), cc-pVTZ, and cc-pVTZ-aug(O)] led to the best agreement with the diffraction-based geometries of **4** and **5** more often than M062X calculations (Tables S12−S17 and S19−S21, Supporting Information). Also, bond and torsional angles predicted by MP2 and M062X showed better agreement with the crystallographic data than those from HF and B3LYP calculations. The overall improvement in bond and torsional angles on raising the level of theory indicates that the use of the solid-state structures derived from the diffraction measurements could, in principle,

provide a reasonable reference point for comparing the performance of QM methods in reproducing geometric characteristics, provided that intermolecular interactions in the solid state are not significant (e.g., in bullvalene). However, the results also suggest that the improvements achieved at higher levels of theory are not significant, especially when considered against the computational time requirements (Table S9, Supporting Information). In cases when molecules larger than **3**−**5** are of interest, M062X calculations (or similar) can provide sufficiently accurate molecular geometries at the final stage of the NMR/MD/QM analysis.

As X-ray structures are often used for rationalizing chemical reactivity or pharmacological activity of small molecules in solution, the question arises whether the diffraction method in the solid state or the NMR/MD/QM analysis provides a better approximation to the solution-state structures. As molecules are no longer held together by intermolecular interactions in solutions and translate rapidly, interchanging their solvent environment continuously, their solution-state structures are likely to be approximated better by the NMR/MD/QM analysis than by diffraction techniques.[62] The downside of the QM-derived structures is that they reflect equilibrium nuclear positions in the minimum of the potential energy surface for a motionless molecule and neglect the effect of thermal averaging at ambient temperatures and that solvation effects are treated implicitly. It is likely that thermal averaging effects in general and solvation effects in nonpolar solvents in particular will cause only insignificant alterations in molecular geometries. Further detailed studies are needed to assess the significance of both of these effects. Within these limitations of the NMR/MD/QM analysis in its present form, a comprehensive verification of the reproducibility of experimentally measured parameters at ambient temperatures is therefore crucial for ensuring the reliability of the structures predicted by the combined approach.

ASSOCIATED CONTENT

S **Supporting Information.** Further results of NMR measurements (NMR spectra; fitted spectra using full line shape analysis; tables including experimentally measured chemical shifts, *J* couplings, and internuclear distances from NOE measurements), MD simulations (distributions of endocyclic torsional angles and interatomic distances), QM calculations (bar charts comparing the performance of QM methods in reproducing experimental molecular geometries; tables including geometries and relative free energies of structures after geometry optimizations and frequency calculations; QM-predicted *J* couplings, internuclear distances, and chemical shifts), and NBO analysis (structural, electronic, and energetic parameters relevant to noncovalent interactions). This material is available free of charge via the Internet at http://pubs.acs.org.

AUTHOR INFORMATION

Corresponding Author
*E-mail: A.E.Aliev@ucl.ac.uk.

ACKNOWLEDGMENT

REFERENCES

(1) (a) Wüthrich, K. *Science* **1989**, *243*, 45. (b) Herrmann, T.; Güntert, P.; Wüthrich, K. *J. Mol. Biol.* **2002**, *319*, 209. (c) Wüthrich, K. *Angew. Chem., Int. Ed.* **2003**, *42*, 3340. (d) Volk, J.; Herrmann, T.; Wüthrich, K. *J. Biomol. NMR* **2008**, *41*, 127. (e) Wüthrich, K. *NMR in Structural Biology*; World Scientific: Singapore, 1995. (f) Wang, X; Lee, H.-W.; Liu, Y. Z.; Prestegard, J. H. *J. Struct. Biol.* **2011**, *173*, 515. (i) Wang, X; Lee, H.-W.; Liu, Y. Z.; Prestegard, J. H. *J. Struct. Biol.* **2011**, *173*, 515. (g) McDermott, A. *Annu. Rev. Biophys.* **2009**, *38*, 385. (h) Tycko, R. *Annu. Rev. Phys. Chem.* **2011**, *62*, 279.

(2) (a) Neuhaus, D.; Williamson, M. P. *The Nuclear Overhauser Effect in Structural and Conformational Analysis*, 2nd ed.; Wiley-VCH: New York, 2000. (b) Claridge, T. *High-Resolution NMR Techniques in Organic Chemistry*; Tetrahedron Organic Chemistry Series; Pergamon Press: Oxford, U.K., 1999; Vol. 19. (c) Reggelin, M.; Hoffman, H.; Köck, M.; Mierke, D. F. *J. Am. Chem. Soc.* **1992**, *114*, 3272.

(3) (a) Chesnut, D. B. The *Ab Initio* Computation of Nuclear Magnetic Resonance Chemical Shielding. In *Reviews in Computational Chemistry*; Lipkowitz, K. B.; Boyd, D. B., Eds.; Wiley-VCH: New York, 1996; Vol. 8, Chapter 5. (b) Helgaker, T.; Jaszuński, M.; Ruud, K. *Chem. Rev.* **1999**, *99*, 293. (c) Kaupp, M., Bühl, M., Malkin, V. G., Eds. *Calculation of NMR and EPR Parameters*; Wiley-VCH: Weinheim, Germany, 2004; (d) Smith, S. G.; Goodman, J. M. *J. Am. Chem. Soc.* **2010**, *132*, 12946. (e) Atieh, Z.; Allouche, A. R.; Lazariev, A.; Van Ormondt, D.; Graveron-Demilly, D.; Aubert-Frécon, M. *Chem. Phys. Lett.* **2010**, *492*, 297.

(4) (a) Bifulco, G.; Bassarello, C.; Riccio, R.; Gomez-Paloma, L. *Org. Lett.* **2004**, *6*, 1025. (b) Krivdin, L. B.; Contreras, R. H. *Annu. Rep. NMR Spectrosc.* **2007**, *61*, 133. (c) Bagno, A.; Saielli, G. *Theor. Chem. Acc.* **2007**, *117*, 603. (d) Helgaker, T.; Jaszuński, M.; Pecul, M. *Prog. Nucl. Magn. Reson. Spectrosc.* **2008**, *53*, 249. (e) Yongye, A. B.; Lachele Foley, B.; Woods, R. J. *J. Phys. Chem. A* **2008**, *112*, 2634. (f) Di Micco, S.; Chini, M. G.; Riccio, R.; Bifulco, G. *Eur. J. Org. Chem.* **2010**, 1411. (g) Taha, H. A.; Castillo, N. C.; Sears, D. N.; Wasylishen, R. E.; Lowary, T. L.; Roy, P.-N. *J. Chem. Theory Comput.* **2010**, *6*, 212. (h) Bally, T.; Rablen, P. R. *J. Org. Chem.* **2011**, *76*, 4818.

(5) Aliev, A. E.; Courtier-Murias, D.; Bhandal, S.; Zhou, S. *Chem. Commun.* **2010**, *46*, 695.

(6) (a) Schmidt, J. M.; Brüschweiler, R.; Ernst, R. R.; Dunbrack, R. L.; Joseph, D.; Karplus, M. *J. Am. Chem. Soc.* **1993**, *115*, 8747. (b) Brunne, R. M.; van Gunsteren, W. F.; Brüschweiler, R.; Ernst, R. R. *J. Am. Chem. Soc.* **1993**, *115*, 4764. (c) Mu, Y.; Kosov, D. S.; Stock, G. *J. Phys. Chem. B* **2003**, *107*, 5064. (d) Hu, H.; Elstner, M.; Hermans, J. *Proteins* **2003**, *50*, 451. (e) Mu, Y.; Kosov, D. S.; Stock, G. *J. Phys. Chem. B* **2003**, *107*, 5064. (f) Mackerell, A. D., Jr. *J. Comput. Chem.* **2004**, *25*, 1584. (g) Kaminský, J.; Jensen, F. *J. Chem. Theory Comput.* **2007**, *3*, 1774. (h) Showalter, S. A.; Brüschweiler, R. *J. Chem. Theory Comput.* **2007**, *3*, 961. (i) Mobley, D. L.; Dumont, É; Chodera, J. D.; Dill, K. A. *J. Phys. Chem. B* **2007**, *111*, 2242. (j) Best, R. B.; Buchete, N.-V.; Hummer, G. *Biophys. J.* **2008**, *95*, L07. (k) Wickstrom, L.; Okur, A.; Simmerling, C. *Biophys. J.* **2009**, *97*, 853. (l) Seabra, G. M.; Walker, R. C.; Roitberg, A. E. *J. Phys. Chem. A* **2009**, *113*, 11938. (m) Project, E.; Nachliel, E.; Gutman, M. *J. Comput. Chem.* **2010**, *31*, 1864. (n) Aliev, A. E.; Courtier-Murias, D. *J. Phys. Chem. B* **2010**, *114*, 12358. (o) Lewandowska, A.; Carmichael, I.; Hörner, G.; Hug, G. L.; Marciniak, B. *Chem. Phys. Lett.* **2011**, *512*, 123.

(7) King, F. D.; Aliev, A. E.; Caddick, S.; Tocher, D. A.; Courtier-Murias, D. *Org. Biomol. Chem.* **2009**, *7*, 167.

(8) Kgomo, D. B.; Levendis, D. C.; Gukasov, A.; Cousson, A.; Schöning, L. F. R.; Venter, A. M. *Acta Crystallogr.* **2005**, *E61*, o1141.

(9) (a) Kumaradhas, P.; Levendis, D. C.; Koritsanszky, T. *Acta Crystallogr.* **2000**, *C56*, 93. (b) Qian, H.-F. *J. Nanjing Univ. Technol.* **2004**, *26*, 35. (c) Wichmann, K.; Bradaczek, H.; Dauter, Z.; Polonski, T. *Acta Crystallogr.* **1987**, *C43*, 577.

(10) Luger, P.; Buschmann, J.; McMullan, R. K.; Ruble, J. R.; Matias, P.; Jeffrey, G. A. *J. Am. Chem. Soc.* **1986**, *108*, 7825.

(11) Koritsanszky, T.; Buschmann, J.; Luger, P.; McMullan, R. K.; Ruble, J. R.; Matias, P.; Jeffrey, G. A. *J. Phys. Chem.* **1996**, *100*, 10547.

1107

dx.doi.org/10.1021/jp211083f |*J. Phys. Chem. A* 2012, 116, 1093–1109

(12) See, for example: Lafitte, V. G. H.; Aliev, A. E.; Horton, P. N.; Hursthouse, M. B.; Hailes, H. C. *Chem. Commun.* **2006**, *20*, 2173.

(13) (a) Williamson, M. P.; Asakura, T. *J. Magn. Reson. B* **1993**, *101*, 63. (b) Osapay, K.; Case, D. A. *J. Am. Chem. Soc.* **1991**, *113*, 9436. (c) Xu, X. P.; Case, D. A. *Biopolymers* **2002**, *65*, 408. (d) Li, D.-W.; Brüschweiler, R. *J. Phys. Chem. Lett.* **2010**, *1*, 246. (e) Hu, J.-S.; Bax, A. *J. Am. Chem. Soc.* **1997**, *119*, 6360. (f) Schmidt, J. M.; Blümel, M.; Löhr, F.; Rüterjans, H. *J. Biomol. NMR* **1999**, *14*, 1.

(14) (a) Gottlieb, H. E.; Kotlyar, V.; Nudelman, A. *J. Org. Chem.* **1997**, *62*, 7512. (b) Fulmer, G. R.; Miller, A. J. M.; Sherden, N. H.; Gottlieb, H. E.; Nudelman, A.; Stoltz, B. M.; Bercaw, J. E.; Goldberg, K. I. *Organometallics* **2010**, *29*, 2176.

(15) Braun, S.; Kalinowski, H.-O.; Berger, S. *150 and More Basic NMR Experiments*, 2nd ed.; Wiley-VCH: Weinheim, Germany, 1998.

(16) *gNMR*, version 5.0.6; NMR Simulation Program; Budzelaar, P. H. M., Ed., 2006.

(17) (a) Haasnoot, C. A. G.; DeLeeuw, F. A. A. M.; DeLeew, H. P. M.; Altona, C. *Biopolymers* **1981**, *20*, 1211. (b) Aliev, A. E.; Courtier-Murias, D. *J. Phys. Chem. B* **2007**, *111*, 14034.

(18) (a) Press, W. H.; Flannery, B. P.; Teukolsky, S. A. *Numerical Recipes in FORTRAN: The Art of Scientific Computing*; Cambridge University Press: Cambridge, U.K., 1992. (b) Aliev, A. E.; Harris, K. D. M. *Magn. Reson. Chem.* **1998**, *36*, 855.

(19) Haasnoot, C. A. G.; DeLeeuw, F. A. A. M.; Altona, C. *Tetrahedron* **1980**, *36*, 2783.

(20) Karplus, M. *J. Am. Chem. Soc.* **1963**, *85*, 2870.

(21) Huster, D.; Arnold, K.; Gawrisch, K. *J. Phys. Chem. B* **1999**, *103*, 243.

(22) Schlecht, M. F. *Molecular Modeling on the PC*; Wiley-VCH: New York, 1998. Software used: *PCMODEL*, version 8.5; Serena Software: Redwood City, CA, 2003.

(23) Case, D. A.; Darden, T. A.; Cheatham T. E., III; Simmerling, C. L.; Wang, J.; Duke, R. E.; Luo, R.; Crowley, M.; Walker, R. C.; Zhang, W.; Merz, K. M.; Wang, B.; Hayik, S.; Roitberg, A.; Seabra, G.; Kolossvary, I.; Wong, K. F.; Paesani, F.; Vanicek, J.; Wu, X.; Brozell, S. R.; Steinbrecher, T.; Gohlke, H.; Yang, L.; Tan, C.; Mongan, J.; Hornak, V.; Cui, G.; Mathews, D. H.; Seetin, M. G.; Sagui, C.; Babin, V.; Kollman, P. A. *AMBER 10*; University of California: San Francisco, CA, 2008.

(24) Wang, J.; Wolf, R. M.; Caldwell, J. W.; Kollman, P. A.; Case, D. A. *J. Comput. Chem.* **2004**, *25*, 1157.

(25) (a) Tsui, V.; Case, D. A. *Biopolymers* **2001**, *56*, 275. (b) Tsui, V.; Case, D. A. *J. Am. Chem. Soc.* **2000**, *122*, 2489. (c) Pellegrini, E.; Field, M. J. *J. Phys. Chem. A* **2002**, *106*, 1316.

(26) Elstner, M.; Porezag, D.; Jungnickel, G.; Elsner, J.; Haugk, M.; Frauenheim, T.; Suhai, S.; Seifert, G. *Phys. Rev. B* **1998**, *58*, 7260.

(27) Jakalian, A.; Bush, B. L.; Jack, D. B.; Bayly, C. I. *J. Comput. Chem.* **2000**, *21*, 132.

(28) Frisch, M. J.; Trucks, G. W.; Schlegel, H. B.; Scuseria, G. E.; Robb, M. A.; Cheeseman, J. R.; Scalmani, G.; Barone, V.; Mennucci, B.; Petersson, G. A.; Nakatsuji, H.; Caricato, M.; Li, X.; Hratchian, H. P.; Izmaylov, A. F.; Bloino, J.; Zheng, G.; Sonnenberg, J. L.; Hada, M.; Ehara, M.; Toyota, K.; Fukuda, R.; Hasegawa, J.; Ishida, M.; Nakajima, T.; Honda, Y.; Kitao, O.; Nakai, H.; Vreven, T.; Montgomery, J. A., Jr.; Peralta, J. E.; Ogliaro, F.; Bearpark, M.; Heyd, J. J.; Brothers, E.; Kudin, K. N.; Staroverov, V. N.; Kobayashi, R.; Normand, J.; Raghavachari, K.; Rendell, A.; Burant, J. C.; Iyengar, S. S.; Tomasi, J.; Cossi, M.; Rega, N. ; Millam, J. M.; Klene, M.; Knox, J. E.; Cross, J. B.; Bakken, V.; Adamo, C; Jaramillo, J.; Gomperts, R. E.; Stratmann, O.; Yazyev, A. J.; Austin, R.; Cammi, C.; Pomelli, J. W.; Ochterski, R.; Martin, R. L.; Morokuma, K.; Zakrzewski, V. G.; Voth, G. A.; Salvador, P.; Dannenberg, J.J.; Dapprich, S.; Daniels, A. D.; Farkas, O.; Foresman, J. B.; Ortiz, J. V.; Cioslowski, J.; Fox, D. J. *Gaussian 09*, revision A.02; Gaussian Inc.: Wallingford, CT, 2009.

(29) Cheeseman, J. R.; Trucks, G. W.; Keith, T. A.; Frisch, M. J. *J. Chem. Phys.* **1996**, *104*, 5497.

(30) (a) Cances, E.; Mennucci, B. *J. Math. Chem.* **1998**, *23*, 309. (b) Cossi, M.; Rega, N.; Scalmani, G.; Barone, V. *J. Comput. Chem.* **2003**, *24*, 669.

(31) Glendening, E. D.; Reed, A. E.; Carpenter, J. E.; Weinhold, F. *NBO*, version 3.1; University of Wisconsin: Madison, WI, 1995.

(32) (a) Stephenson, D.; Binsch, G. *J. Magn. Reson.* **1980**, *37*, 395. (b) Günther, H. *NMR Spectroscopy*, 2nd ed.; Wiley: New York, 1995; (c) Hägele, G.; Engelhardt, M.; Boenigk, M. *Simulation und automatisierte Analyse von Kernresonanzspektren*; VCH: Weinheim, Germany, 1987.

(33) (a) Allen, F. H. *Acta Crystallogr.* **1986**, *B42*, 515. (b) Allen, F. H.; Bruno, I. J. *Acta Crystallogr.* **2010**, *B66*, 380. (c) Wilson, C. C. *Single Crystal Neutron Diffraction From Molecular Materials*; World Scientific: Singapore, 2000.

(34) We used the previously suggested notation,[7,17] where the endo/exo orientation of the C_4 and C_8 atoms is determined relative to the C_2—C_1 bond.

(35) For the major conformer **3a**, the MP2/6-31+G(d) calculations identify 14 minima (all with 0 imaginary frequencies) with relative energies varying between 0 and 0.0788 kJ mol^{-1}, because the convergence condition used in these calculations was less tight than in other sets of calculations (see Experimental Section). However, the variation range is negligibly small.

(36) (a) Margulès, L.; Demaison, J.; Boggs, J. E. *J. Mol. Struct. (THEOCHEM)* **2000**, *500*, 245. (b) Wang, N. X.; Wilson, A. K. *J. Chem. Phys.* **2004**, *121*, 7632. (c) Riley, K. E.; Op't Holt, B. T.; Merz, K. M., Jr. *J. Chem. Theory Comput.* **2007**, *3*, 407.

(37) (a) Becke, A. D. *J. Chem. Phys.* **1993**, *98*, 5648. (b) Lee, C.; Yang, W.; Parr, R. G. *Phys. Rev. B* **1988**, *37*, 785.

(38) (a) Zhao, Y.; Truhlar, D. G. *Theor. Chem. Acc.* **2008**, *120*, 215. (b) Zhao, Y.; Truhlar, D. G. *J. Chem. Theory Comput.* **2008**, *4*, 1849.

(39) Head-Gordon, M.; Pople, J. A.; Frisch, M. J. *Chem. Phys. Lett.* **1988**, *153*, 503.

(40) (a) Hargittai, M.; Hargittai, I. *Int. J. Quantum Chem.* **1992**, *44*, 1057. (b) Ma, B.; Lii, J.-H.; Schaefer, H. F., III; Allinger, N. L. *J. Phys. Chem.* **1996**, *100*, 8763. (c) Hargittai, M. *Chem. Rev.* **2000**, *100*, 2233.

(41) (a) Cramer, C. J. *Essentials of Computational Chemistry*; John Wiley & Sons: Chichester, U.K., 2002. (b) Purvis, G. D., III; Bartlett, R. J. *J. Chem. Phys.* **1982**, *76*, 1910. (c) Scuseria, G. E.; Janssen, C. L.; Schaefer, H. F., III. *J. Chem. Phys.* **1988**, *89*, 7382.

(42) For discrepancies between XRD and ND geometric parameters of non-hydrogen atoms and the discussion of the role of asphericity effects, see ref 33a. Note that the large differences between the neutron and X-ray diffraction bond lengths might be caused by the less accurate cell parameter determination in the case of neutron diffraction measurements.

(43) Kayushina, K. L.; Vainshtein, B. K. *Sov. Phys. Crystallogr.* **1965**, *10*, 698.

(44) With the exception of a few special cases, the methyl group rotation is retained in the solid state. Therefore, unlike intermolecular noncovalent interactions and flexible ring dynamics, the methyl group rotation is not expected to lead to large deviations in solid and solution-state structures, although further model studies might be required to assess its influence on molecular geometries.

(45) (a) Simandiras, E. D.; Handy, N. C.; Amos, R. D. *Chem. Phys. Lett.* **1987**, *133*, 324. (b) Bauschlicher, C. W., Jr. *Chem. Phys. Lett.* **1995**, *246*, 40. (c) Sousa, S. F.; Fernandes, P. A.; Ramos, M. J. *J. Phys. Chem. A* **2007**, *111*, 10439.

(46) (a) Murphy, R. B.; Beach, M. D.; Friesner, R. A.; Ringnalda, M. N. *J. Chem. Phys.* **1995**, *103*, 1481. (b) Friesner, R. A. *Proc. Natl. Acad. Sci. U.S.A.* **2005**, *102*, 6648. (c) Grimme, S. *Angew. Chem., Int. Ed.* **2006**, *45*, 4460. (d) Grimme, S.; Mück-Lichtenfeld, C. *Chirality* **2008**, *20*, 1009.

(47) (a) Echenique, P.; Alonso, J. L. *J. Comput. Chem.* **2008**, *29*, 1408. (b) Aliev, A. E.; Bhandal, S.; Courtier-Murias, D. *J. Phys. Chem. A* **2009**, *113*, 10858.

(48) Shen, Y.; Bax, A. *J. Biomol. NMR* **2007**, *38*, 289.

(49) (a) Forsyth, D. A.; Sebag, A. B. *J. Am. Chem. Soc.* **1997**, *119*, 9483. (b) Rablen, P. R.; Pearlman, S. A.; Finkbiner, J. *J. Phys. Chem. A* **1999**, *103*, 7357. (c) Baldridge, K. K.; Siegel, J. S. *J. Phys. Chem. A* **1999**, *103*, 4038. (d) Aliev, A. E.; Courtier-Murias, D.; Zhou, S. *J. Mol. Struct. (THEOCHEM)* **2009**, *893*, 1. (e) Jain, R.; Bally, T.; Rablen, P. R. *J. Org. Chem.* **2009**, *74*, 4017. (f) Sarotti, A. M.; Pellegrinet, S. C. *J. Org.*

1108

dx.doi.org/10.1021/jp211083f | *J. Phys. Chem. A* 2012, 116, 1093–1109

Chem. **2009**, *74*, 7254. (g) Pankratyev, E. Y.; Tulyabaev, A. R.; Khalilov, L. M. *J. Comput. Chem.* **2011**, *32*, 1993.

(50) (a) Müller-Dethlefs, K.; Hobza, P. *Chem. Rev.* **2000**, *100*, 143. (b) Jennings, W. B.; Farrell, B. M.; Malone, J. F. *Acc. Chem. Res.* **2001**, *34*, 885. (c) Steiner, T. *Angew. Chem., Int. Ed. Engl.* **2002**, *41*, 48. (d) Meyer, E. A.; Castellano, R. K.; Diederich, F. *Angew. Chem., Int. Ed. Engl.* **2003**, *42*, 1210. (e) Aliev, A. E.; Harris, K. D. M. *Struct. Bonding (Berlin)* **2004**, *108*, 1. (f) Tsuzuki, S *Struc. Bond* **2005**, *115*, 149. (g) Černý, J.; Hobza, P. *Phys. Chem. Chem. Phys.* **2007**, *9*, 5291. (h) Zhao, Y.; Truhlar, D. G. *J. Chem. Theory Comput.* **2007**, *3*, 289. (i) Dunitz, J. D.; Gavezzotti, A. *Chem. Soc. Rev.* **2009**, *38*, 2622. (j) Nishio, M.; Umezawa, Y.; Honda, K.; Tsuboyamad, S.; Suezawa, H. *CrystEngComm* **2009**, *11*, 1757. (k) Takahashi, O.; Kohno, Y.; Nishio, M. *Chem. Rev.* **2010**, *110*, 6049.

(51) (a) Branden, C.; Tooze, J. *Introduction to Protein Structure*; Garland Publishing: New York, 1999. (b) Lafitte, V. G. H.; Aliev, A. E.; Horton, P. N.; Hursthouse, M. B.; Bala, K.; Golding, P.; Hailes, H. C. *J. Am. Chem. Soc.* **2006**, *128*, 6544 and references therein.

(52) (a) Kitaygorodsky, A. I. *Molecular Crystals and Molecules*; Academic Press: New York, 1973; (b) Israelachvili, J. N. *Intermolecular and Surface Forces*; Academic Press: San Diego, 1992.

(53) Atkinson, C. E.; Aliev, A. E.; Motherwell, W. B. *Chem.—Eur. J.* **2003**, *9*, 1714.

(54) Taylor, R.; Kennard, O. *J. Am. Chem. Soc.* **1982**, *104*, 5063.

(55) Aliev, A. E.; Moïse, J.; Motherwell, W. B.; Nič, M.; Courtier-Murias, D.; Tocher, D. A. *Phys. Chem. Chem. Phys.* **2009**, *11*, 97.

(56) (a) Alekseyeva, E. S.; Batsanov, A. S.; Boyd, L. A.; Fox, M. A.; Hibbert, T. G.; Howard, J. A. K.; MacBride, J. A. H.; MacKinnon, A.; Wade, K. *J. Chem. Soc., Dalton Trans.* **2003**, 475. (b) Cappelli, A.; Giorgi, G.; Anzini, M.; Vomero, S.; Ristori, S.; Rossi, C.; Donati, A. *Chem.—Eur. J.* **2004**, *10*, 3177. (c) Afonin, A. V.; Ushakov, I. A.; Vashchenko, A. V.; Simonenko, D. E.; Ivanov, A. V.; Vasil'tso, A. M.; Mikhaleva, A. I.; Trofimov, B. A. *Magn. Reson. Chem.* **2009**, *47*, 105.

(57) Wong, N.-B.; Cheung, Y.-S.; Wu, D. Y.; Ren, Y.; Wang, X.; Tian, A. M.; Li, W.-K. *J. Mol. Struct. (THEOCHEM)* **2000**, *507*, 153.

(58) Hobza, P.; Havlas, Z. *Chem. Rev.* **2000**, *100*, 4253.

(59) Regarding hyperconjugation and the $n \rightarrow \sigma^*(C—H)$ delocalization, see: (a) Reed, A. E.; Weinhold, F. *J. Chem. Phys.* **1985**, *83*, 1736. (b) Alabugin, I. V.; Manoharan, M.; Peabody, S.; Weinhold, F. *J. Am. Chem. Soc.* **2003**, *125*, 5973. (c) Chocholoušová, J.; Špirko, V.; Hobza, P. *Phys. Chem. Chem. Phys.* **2004**, *6*, 37.

(60) As an example of using a posteriori linear scaling of calculated $^3J_{HH}$ couplings in a manner similar to that described in this work for NMR chemical shifts, the rms$_J$ deviations for seven different calculations of **3** reduce from 0.75−0.82 Hz (Tables S34-S40, Supporting Information) to 0.42−0.45 Hz.

(61) Jacobsen, H. *J. Chem. Theory Comput.* **2011**, *7*, 3019.

(62) See, for example, Table 6 in ref 17b, showing that the geometry of L-proline in D_2O from the NMR analysis agrees better with the QM-predicted geometry than the XRD geometry.